









NUMERICAL MODELLING AND INVERSION OF BOREHOLE  
INDUCED POLARIZATION DATA

by

Amir.H. Javaheri Koupaei

A THESIS SUBMITTED IN PARTIAL FULFILLMENT OF THE REQUIREMENTS FOR THE  
DEGREE OF MASTER OF SCIENCE  
IN  
EARTH SCIENCE (GEOPHYSICS)  
DEPARTMENT OF EARTH SCIENCES  
FACULTY OF SCIENCES  
MEMORIAL UNIVERSITY OF NEWFOUNDLAND  
ST. JOHN'S, NEWFOUNDLAND

FEBRUARY 2012

© Copyright by Amir.H. Javaheri Koupaei

## **Abstract**

The classical borehole Induced Polarization (IP) for mineral exploration is using a lateral probe where the two potential electrodes and one current electrode are deployed in one probe and used to measure the voltage in the drill-hole while the other current electrode is placed on the ground at infinity. Classical borehole IP has several limitations including an investigation radius that is restricted by borehole depth, depth of measurements limited by borehole depth, sensitivity to in-hole mineralization, and data are not suited to 3D inversion. In the first part of this thesis, numerical modelling and inversion methods for the measurements of a novel IP borehole survey design have been investigated. The new survey design called, hole-to-hole IP, has been introduced by Abitibi Geophysics and aims to compensate the limitations of classical borehole IP especially in providing data that are suitable for 3D modelling and inversion. The geophysical modelling package "DCIP3D" provided by Geophysical Inversion Facility of the University of British Columbia has been used for forward modelling and inversion of hole-to-hole IP data. Different combinations of receivers and boreholes have been examined to obtain the economically optimum survey design including the minimum number of boreholes and receiver locations for a successful imaging of the chargeable ore body in a mineral exploration project. Also, a weighting function has been applied to improve the imaging of the mineral deposit located

between boreholes. In the second part of the thesis, a 3D numerical modelling techniques based on integral equation methods for modelling of DC resistivity and IP data has been developed. The pivotal novelties in the code are, first, the application of unstructured meshes which is more flexible to complicated geometry with respect to the structured mesh. Second, the 3D code has been developed to allow both constant and linearly variable charge inside each cell and this enables us to simulate the charge accumulation over the boundary surface more precisely. Therefore, the developed code will enable numerical modelling to be done for more complicated ore bodies than was previously the case.

## Acknowledgements

It is a pleasure to thank the many people who made this thesis possible. First and foremost, I would like to gratefully and sincerely thank my supervisor Dr. Colin G. Farquharson for his guidance, understanding, patience and most importantly, his friendship during my graduate studies at Memorial University of Newfoundland. He encouraged me to not only grow as a geophysicist but also as an instructor and an independent thinker. I would like to thank Abitibi Geophysics, especially Mr. Pierre Bérubé, for giving me the opportunity to be involved in the development of a new borehole IP method and providing me with the funding, synthetic models, and field data. Also, the generous support from MITACS foundation is greatly appreciated. I would like to thank the Department of Earth Sciences at Memorial University of Newfoundland, especially Dr. Charles A. Hurich as a member of my master committee for his input, valuable discussions and accessibility. I would like to thank the Geophysical Inversion Facility of the University of British Columbia for providing us with the modelling package "DCIP3D". Furthermore, Dr. Peter Lelièvre has always been a good friend and I appreciate all his help in coding techniques and dealing with the unstructured meshes. My deepest gratitude goes to my parents for their faith in me and allowing me to be as ambitious as I wanted. It was under their watchful eyes that I gained so much drive and an ability to tackle challenges head on. Finally, and most importantly,

I would like to thank my wife Naziheh. Her support, encouragement, quiet patience and unwavering love were undeniably the bedrock upon which the past two years of my life have been built.

## Table of Contents

<b>Abstract</b>	<b>ii</b>
<b>Acknowledgements</b>	<b>iv</b>
<b>List of Figures</b>	<b>xi</b>
<b>Chapter 1 Introduction</b>	<b>1</b>
<b>Chapter 2 Electrical Methods</b>	<b>4</b>
2.1 The DC Resistivity Method . . . . .	4
2.1.1 Introduction . . . . .	4
2.1.2 Resistivity basics . . . . .	5
2.1.3 Potential in homogeneous media . . . . .	6
2.1.4 Single current electrode at depth . . . . .	8
2.1.5 Single current electrode at the Earth's surface . . . . .	10
2.1.6 Two current electrodes at the surface . . . . .	11
2.1.7 Borehole DC resistivity methods . . . . .	13
2.1.7.1 Single borehole survey . . . . .	13
2.1.7.2 Cross-borehole surveys . . . . .	14
2.2 The Induced Polarization Method . . . . .	15

2.2.1	Introduction . . . . .	15
2.2.2	Sources of Induced Polarization . . . . .	17
2.2.2.1	Electrode Polarization . . . . .	17
2.2.2.2	Membrane Polarization . . . . .	18
2.2.3	Measuring the IP Effect in Time Domain . . . . .	19
2.2.3.1	Polarizability . . . . .	19
2.2.3.2	Chargeability . . . . .	20
2.2.4	Measuring the IP Effect in Frequency Domain . . . . .	20
2.2.4.1	Percentage frequency effect, PFE . . . . .	20
2.2.4.2	Metal Factor . . . . .	21
2.2.4.3	Phase Shift . . . . .	21
2.2.5	Borehole IP Methods . . . . .	22
2.2.5.1	Classical Borehole IP . . . . .	22
2.2.5.2	Hole-to-hole IP survey . . . . .	23
<b>Chapter 3</b>	<b>3D Forward Modelling and Inversion of IP - Theory</b>	<b>25</b>
3.1	3D Forward modelling of IP data . . . . .	25
3.2	3D Inversion of IP data . . . . .	27
3.2.1	Inversion of DC resistivity data: Gauss-Newton Method . . . . .	30
3.2.2	IP Inversion . . . . .	31
<b>Chapter 4</b>	<b>Survey design for hole-to-hole IP data - modelling and</b>	

	<b>inversion study</b>	<b>34</b>
4.1	3D mesh design . . . . .	34
4.2	Example 1: Single Chargeable body . . . . .	35
4.2.1	Mesh design and forward modelling accuracy test . . . . .	36
4.2.2	Inversion of data from different boreholes combinations . . . . .	45
4.2.2.1	Inversion of data from boreholes F1 and F2 . . . . .	45
4.2.2.2	Inversion of data from boreholes F1, F2 and F3 . . . . .	50
4.2.2.3	Inversion of data from boreholes F1, F2 and F4 . . . . .	53
4.2.2.4	Inversion of data from boreholes F1, F2 and F5 . . . . .	56
4.2.2.5	Inversion of data from boreholes F1, F2, F3, F4 and F5 . . . . .	59
4.2.2.6	Inversion of data from all boreholes . . . . .	62
4.2.2.7	Borehole pairs without anomaly . . . . .	65
4.2.2.8	Vertical Borehole pair not straddling the anomaly . . . . .	70
4.2.3	Distance weighting function . . . . .	75
4.3	Example 2: Aurbel project . . . . .	78
4.3.1	Forward modelling . . . . .	78
4.3.2	Inversion of the field data . . . . .	82
<b>Chapter 5</b>	<b>3D DC Resistivity and IP Forward Modelling based on</b>	
	<b>a Surface Integral Equation</b>	<b>88</b>
5.1	Introduction . . . . .	88

5.2	IP numerical modelling . . . . .	90
5.2.1	Siegel's Theory . . . . .	91
5.3	Formulating the Surface Integral equation . . . . .	93
5.3.1	Charge accumulation and Poisson's equation for the potential . . . . .	94
5.3.2	A Surface Integral Equation for the charge density . . . . .	98
5.3.3	Singularity removal . . . . .	100
5.4	3D Surface integral equation forward modelling code . . . . .	101
5.4.1	Numerical calculation of a surface integral over an arbitrary 3D triangle . . . . .	102
5.4.2	3D forward modelling code for piecewise constant electric charge	108
5.4.3	3D forward modelling code for linearly varying electric charge	110
5.5	Example 1: Potential due to a buried conductive sphere . . . . .	113
5.5.1	Analytical formula for the potential due to a sphere in a uniform field . . . . .	113
5.5.2	3D Numerical solution for the potential due to a sphere in a uniform field . . . . .	115
5.5.2.1	Charge Accumulation over the 3D spherical anomaly	116
5.5.2.2	Different location of current source . . . . .	118
5.5.2.3	Discretization effect on calculated potential . . . . .	121
5.5.2.4	Different orders of integration . . . . .	124
5.6	Example 2: Potential due to a buried conductive prism . . . . .	127

5.7 IP response due to a buried polarisable prism . . . . .	135
<b>Chapter 6 Conclusion</b>	<b>138</b>
<b>Bibliography</b>	<b>140</b>
<b>Appendices</b>	<b>147</b>

## List of Figures

2.1	Resistivity vs. resistance (Boyed, 2003). . . . .	5
2.2	Current flow and Ohm's Law (Boyed, 2003). . . . .	6
2.3	Buried point source of current in homogeneous medium (Telford et al., 1976). . . . .	9
2.4	Point source of current at the surface of homogeneous medium (Telford et al., 1976). . . . .	10
2.5	Two current and two potential electrodes on the surface of a homogeneous isotropic ground of resistivity $\rho$ (Telford et al., 1976). . . . .	11
2.6	Plan view of equipotentials and current flow-lines for two point sources of current on a homogeneous half-space (Dobrin, 1960). . . . .	12
2.7	Common arrays used in surface resistivity surveys and their geometric factors (Loke, 1999). . . . .	13
2.8	Mise-à-la-masse array (Rubin and Hubbard, 2005). . . . .	14
2.9	Measurement configuration for cross-borehole resistivity imaging. Electrodes A and B are for current injection, M and N are for voltage measurement. Scheme (a) is AM-BN and scheme (b) is AB-MN (Rubin et al., 2005). . . . .	15

2.10	Typical current and idealized voltage wave forms for field DC resistivity surveys. $V_p$ is the primary voltage and $V_{sp}$ is observed self-potential voltage (Rubin and Hubbard, 2005). . . . .	16
2.11	Phenomenon of induced polarization (Parasnis, 1997). . . . .	17
2.12	(a) Electrode polarization phenomenon at mineral-electrolyte interfaces. (b) Membrane polarization phenomenon in clays (Sharma, 1997). . . . .	17
2.13	(a) Normal and (b) lateral probes used in classical borehole IP (Kaufman and Anderson, 2010). . . . .	23
2.14	Hole-to-hole IP array, (Berube, 2010). . . . .	24
3.1	IP effect in Time domain (DCIP3D Manual, UBC-GIF). . . . .	26
4.1	Oblique 3D view of all drill holes, current electrodes and the chargeable body for the first example model. . . . .	36
4.2	Plan view of the 7 drillholes and chargeable body. . . . .	37
4.3	DC potential measurements over the Earth model, Mesh A (blue circles) and Mesh B (red triangles). Other lines correspond to the designed meshes with different dimension and cell size. . . . .	38
4.4	Calculated IP values (dimensionless chargeability) for the Earth model using Mesh A (blue circles) and Mesh B (red triangles). . . . .	39

4.5	Running time of the forward modelling program DCIPF3D as a function of the number of cells in the mesh. . . . .	40
4.6	Calculated potential in Volts in Mesh A, 3D view. . . . .	40
4.7	Calculated potential in Volts in Mesh A, plan view. . . . .	41
4.8	Location of the two current electrodes, Mesh A, showing the cells in the model. . . . .	41
4.9	Mesh A, 3D view. . . . .	42
4.10	Calculated potential in Volts in Mesh B, 3D view. . . . .	42
4.11	Calculated Potential in Mesh B, plan view. . . . .	43
4.12	Location of the two current electrodes, Mesh B, showing the cells in the model. . . . .	43
4.13	Mesh B, 3D view. . . . .	44
4.14	IP sensitivity matrix, $J$ , for boreholes F1 and F2 where the true model is shown via transparency. The color scale represents the cumulative value of sensitivity in each cell. . . . .	46
4.15	Chargeability model constructed of data from boreholes F1 and F2 using mesh A, finer mesh, where the true model is shown via transparency. The color scale represent the values of dimensionless chargeability. . . . .	47

4.16	Chargeability model constructed from data from boreholes F1 and F2 using mesh B, coarser mesh, where the true model is shown via transparency. The color scale represent the values of dimensionless chargeability. . . . .	48
4.17	Synthetic observed data (blue dots) and predicted data (red line) for the chargeability model derived from F1-F2 data. . .	49
4.18	IP sensitivity matrix for boreholes F1, F2 and F3 where the true model is shown via transparency. The color scale represents the cumulative value of sensitivity in each cell. . . . .	50
4.19	Chargeability model constructed from data from boreholes F1, F2 and F3 using mesh B where the true model is shown via transparency. The color scale represent the values of dimensionless chargeability. . . . .	51
4.20	Synthetic observed data (blue) and predicted data (red) for the chargeability model derived from F1, F2 and F3 data. . . . .	52
4.21	IP sensitivity matrix for boreholes F1, F2 and F4 where the true model is shown via transparency. The color scale represents the cumulative value of sensitivity in each cell. . . . .	53

4.22	Chargeability model constructed for data from boreholes F1, F2 and F4 using mesh B where the true model is shown via transparency. The color scale represent the values of dimensionless chargeability. . . . .	54
4.23	Synthetic observed data (blue) and predicted data (red) for the chargeability model derived from F1, F2 and F4 data. . . . .	55
4.24	IP sensitivity matrix for boreholes F1, F2 and F5 where the true model is shown via transparency. The color scale represents the cumulative value of sensitivity in each cell. . . . .	56
4.25	Chargeability model constructed from data from boreholes F1, F2 and F5 using mesh B where the true model is shown via transparency. The color scale represent the values of dimensionless chargeability. . . . .	57
4.26	Synthetic observed data (blue) and predicted data (red) for the chargeability model derived from F1, F2 and F5 data. . . . .	58
4.27	Comparing the results of three hole combination. . . . .	58
4.28	IP sensitivity matrix for boreholes F1, F2, F3, F4 and F5 where the true model is shown via transparency. The color scale represents the cumulative value of sensitivity in each cell. . . . .	59

4.29	Chargeability model constructed of data from boreholes F1, F2, F3, F4 and F5 using mesh B where the true model is shown via transparency. The color scale represent the values of dimensionless chargeability. . . . .	60
4.30	Synthetic observed data (blue) and predicted data (red) for the chargeability model derived from F1, F2, F3, F4 and F5 data . . . . .	61
4.31	IP sensitivity matrix for all boreholes where the true model is shown via transparency. The color scale represents the cumulative value of sensitivity in each cell. . . . .	62
4.32	Chargeability model constructed of data from all boreholes using mesh B where the true model is shown via transparency. The color scale represent the values of dimensionless chargeability. . . . .	63
4.33	Predicted data (red) and synthetic observed data (blue) for the chargeability model derived for data from all bore holes data. . . . .	64
4.34	IP sensitivity matrix for boreholes F7 and F1 where the true model is shown via transparency. The color scale represents the cumulative value of sensitivity in each cell. . . . .	65

4.35	Chargeability model constructed from data from boreholes F7 and F1 using mesh B where the true model is shown via transparency. The color scale represent the values of dimensionless chargeability. . . . .	66
4.36	Synthetic observed data (blue) and Predicted data (red) for the chargeability model derived from F7 and F1 data. . . . .	67
4.37	IP sensitivity matrix for boreholes F2 and F6 where the true model is shown via transparency. The color scale represents the cumulative value of sensitivity in each cell. . . . .	67
4.38	Chargeability model constructed of data from boreholes F2 and F6 using mesh B where the true model is shown via transparency. The color scale represent the values of dimensionless chargeability. Final value of misfit was 77.766. . . . .	68
4.39	Synthetic observed data (blue) and predicted data (red) for the chargeability model derived from F2 and F6 data. . . . .	69
4.40	IP sensitivity matrix. Target body is on the right side of the boreholes can be seen because of transparent overlay of true model. The color scale represents the cumulative value of sensitivity in each cell. . . . .	71

4.41	Chargeability model constructed from data from vertical boreholes using mesh B. The color scale represent the values of dimensionless chargeability. Target body is on the right side. . .	72
4.42	IP sensitivity matrix. Target body is on the left side of the boreholes can be seen because of transparent overlay of true model. The color scale represents the cumulative value of sensitivity in each cell. . . . .	73
4.43	Chargeability model constructed from data from vertical boreholes using mesh B. The color scale represents the values of dimensionless chargeability. Final value of misfit was 65.282. Target body is on the left side. . . . .	74
4.44	Inversion results using the distance weighting function (Mesh B), F1 and F2, Northing = 250. . . . .	76
4.45	Inversion results using the distance weighting function (Mesh B), F1 and F2, Northing = 350. . . . .	76
4.46	Inversion results using the distance weighting function (Mesh B), F1 and F2, Northing = 450. . . . .	77
4.47	Earth synthetic model information for Aurbel property located east of Val-d'Or, Quebec, Canada. . . . .	79
4.48	Plan view of the boreholes in Aurbel area. . . . .	79

4.49	Chargeability model constructed of data from all twelve pair of boreholes using mesh B where the true model is shown via transparency. The color scale represent the values of dimensionless chargeability. . . . .	80
4.50	Synthetic observed data (yellow) and predicted data (red) for the chargeability model derived from data from all boreholes. . . . .	81
4.51	Location of the Aurbel project (Berube, 2010). . . . .	82
4.52	General geology of the area (Berube, 2010). . . . .	83
4.53	An example of noisy data with large variation from boreholes 26-32. . . . .	84
4.54	Synthetic observed data (blue) and Predicted data (red) for the conductivity model derived from all boreholes. . . . .	85
4.55	Chargeability model constructed from the Aurbel data using distance weighting. The color scale represent the values of dimensionless chargeability. . . . .	85
4.56	3D view of the chargeable targets in Aurbel property located east of Val-d'Or, Quebec, Canada. . . . .	86
4.57	Observed data (blue) and predicted data (red) for the Aurbel data-set. . . . .	87
5.1	Volume dipolar element (Seigel, 1959). . . . .	92

5.2	Geometry of the Earth model for the surface integral forward modelling where C and P are the current and potential electrodes respectively and S is the surface of the anomaly (Dieter et al., 1969). . . . .	102
5.3	The surface rotation of the Cartesian system (Okabe 1979) . . .	103
5.4	The projection of a triangular surface (Okabe 1979) . . . . .	105
5.5	Transformation of standard triangle $T$ into equivalent unit square in $(u, v)$ space and 2-square in $(\zeta, \eta)$ space (Rathod et al., 2007).	108
5.6	Buried conducting sphere in uniform field. $a$ is the radius of the sphere, $\rho_2$ is the resistivity of the sphere and $\rho_1$ is the resistivity of the halfspace (Telford et al., 1990). . . . .	113
5.7	Discretized sphere for the example presented in Section 5.5 with 1520 triangular facets and 762 nodes. . . . .	115
5.8	Charge accumulation, in coulomb (C), over a conductive sphere in a resistive background. . . . .	117
5.9	DC resistivity potential due to conductive buried sphere using pole-pole configuration for a source location of $(-50, 350, 0)$ m: analytic response (blue), 3D forward modelling code (orange). . . . .	118
5.10	DC resistivity potential due to conductive buried sphere using pole-pole configuration for a source location of $(-1000, 350, 0)$ m: analytic response (blue), 3D forward modelling code (orange).	119

5.11	DC resistivity potential due to conductive buried sphere using pole-pole configuration for a source location of $(-5000, 350, 0)$ m: analytic response (blue), 3D forward modelling code (orange).	119
5.12	DC resistivity potential due to conductive buried sphere using pole-pole configuration for a source location of $(-10000, 350, 0)$ m: analytic response (blue), 3D forward modelling code (orange).	120
5.13	DC resistivity potential for the conductive buried sphere using a pole-pole configuration and using 94 facets and 49 nodes, analytic response (blue), 3D forward modelling code (orange).	121
5.14	DC resistivity potential for the conductive buried sphere using a pole-pole configuration and using 304 facets and 154 nodes, analytic response (blue), 3D forward modelling code (orange).	122
5.15	DC resistivity potential for the conductive buried sphere using a pole-pole configuration and using 1254 facets and 629 nodes, analytic response (blue), 3D forward modelling code (orange).	122
5.16	DC resistivity potential for the conductive buried sphere using a pole-pole configuration and using 1520 facets and 762 nodes, analytic response (blue), 3D forward modelling code (orange).	123
5.17	Different orders of integration for an sphere discretized into 94 facets and 49 nodes. . . . .	125

5.18	Different orders of integration for an sphere discretized into 1520 facets and 762 nodes. . . . .	126
5.19	Discretized prism using unstructured linear triangular facets with the extension of $x = 1150$ to $1300$ m, $y = 250$ to $450$ m, and $z = -400$ to $-700$ m and discretized into 4106 facets and 2055 nodes. . . . .	128
5.20	DC resistivity potential due to a conductive prism using the pole-pole configuration and observation locations along the $x$ -axis, and 28 facets and 16 nodes: DCIP3D Mesh A (blue), Mesh B (black), 3D Forward modelling code (orange). . . . .	129
5.21	DC resistivity potential due to a conductive prism using the pole-pole configuration and observation locations along the $x$ -axis, and 296 facets and 150 nodes: DCIP3D Mesh A (blue), Mesh B (black), 3D Forward modelling code (orange). . . . .	130
5.22	DC resistivity potential due to a conductive prism using the pole-pole configuration and observation locations along the $x$ -axis, and 2646 facets and 1325 nodes: DCIP3D Mesh A (blue), Mesh B (black), 3D Forward modelling code (orange). . . . .	131

5.23	DC resistivity potential due to a conductive prism using the pole-pole configuration and observation locations along the $x$ -axis, and 3068 facets and 1536 nodes: DCIP3D Mesh A (blue), Mesh B (black), 3D Forward modelling code (orange). . . . .	132
5.24	DC resistivity potential due to a conductive prism using the pole-pole configuration and observation locations along the $x$ -axis, and 4106 facets and 2055 nodes: DCIP3D Mesh A (blue), Mesh B (black), 3D Forward modelling code (orange). . . . .	133
5.25	DC resistivity potential due to a conductive prism using the pole-pole configuration and observation locations along the $x$ -axis, and 5744 facets and 2876 nodes: DCIP3D Mesh A (blue), Mesh B (black), 3D Forward modelling code (orange). . . . .	134
5.26	IP response as secondary potential due to polarisable buried cube using pole-pole configuration, DCIP3D Mesh A (blue), 3D forward modelling code (orange), 4106 facets and 2055 nodes	136
5.27	IP response as secondary potential due to polarisable buried cube using pole-pole configuration, DCIP3D Mesh B (black), 3D forward modelling code (orange), 4106 facets and 2055 nodes	137

## Chapter 1

### Introduction

Although scientific curiosity to obtain a better understanding of the Earth's nature is the major motive in exploring the Earth's surface and its interior, a key motive is the exploration for mineral resources. In the past few decades, improving standards of living have caused more demand for water, fuel and other minerals. Over the past 3 centuries, geophysical techniques have been used in mineral exploration. The first application of geophysics in mineral prospecting was the use of a magnetic compass in searching for iron ore in Sweden, 1640. The Schlumberger brothers successfully applied self potential (SP) and direct current (DC) resistivity methods in the early 1900's. In 1912, Conrad Schlumberger introduced a new technique for mineral exploration called the "Induced Polarization" method and employed the technique for investigation of economic sulphide deposits (Zonge, 1993). Since electrical methods, including the induced polarization (IP) technique, have been shown to be effective in mineral exploration (Fink et al., 1990), there has been much improvement and development both in practical issues such as equipment and theoretical issues such as processing and modelling methods. Downhole techniques were firstly developed for in-hole assaying. Afterwards, to evaluate mineralization and alteration features

between drill-holes, cross-hole tomography was developed (Zonge, 1993). Since then, several configurations for surface DC resistivity and IP have been deployed in boreholes to improve resolution of these methods with depth. Each configuration has its own advantages and limitations. The most common method in borehole IP for mineral exploration is using a lateral probe where the two potential electrodes and one current electrode are deployed in one probe and used to measure the voltage in the drill-hole (Kaufman and Anderson, 2010). The other current electrode is placed on the ground at infinity. I refer to this method as “classical borehole IP”. Classical borehole IP has several limitations including an investigation radius that is restricted by borehole depth, a depth of measurement also limited by borehole depth, and sensitivity to in-hole mineralization. The data are not suited to 3D inversion.

In the first part of this thesis, I investigate via numerical modelling and inversion a novel IP borehole survey design. The new survey design is called hole-to-hole IP in which the current electrodes are placed on the Earth’s surface with a separation at least two times the target depth and the potential electrodes are deployed in two separate boreholes. It was introduced by Abitibi Geophysics and aims to overcome the limitations of classical borehole IP especially by providing data that are suitable for 3D modelling and inversion. After introducing the theoretical concepts of DC resistivity and IP methods for surface and borehole studies in Chapter 2, a short description of the theory of the forward modelling and inversion of DC resistivity and IP data will be given in Chapter 3, in which I have used the modelling package

“DCIP3D” provided by the Geophysical Inversion Facility of the University of British Columbia. In Chapter 4, examples of the 3D inversion of hole-to-hole IP data using DCIP3D will be illustrated where the aim is to determine in particular how few (or how many) electrode locations are required to obtain good inversion results, and in general how the inversion of hole-to-hole data depends on the number and configuration of electrode locations. Finally, the inversion results of hole-to-hole field data will be presented. In the second part of the thesis, a new 3D forward modelling method based on a surface integral equation will be developed for DC resistivity and IP data. The pivotal novelties in the method are, first, the application of unstructured meshes which are more flexible than structured meshes and can thus better represent complicated geometries. Second, the 3D method has been developed for both constant and linearly variable charge inside each cell and this enables the charge accumulation over the boundary surface to be simulated more precisely. Therefore, the developed method will enable numerical modelling to be done for more complicated ore bodies than was previously the case. The complete description of the theoretical and programming aspects of the code will be covered in Chapter 5. The final chapter will present the conclusions. Also, extra detailed information on the code will be found in the Appendix A and Appendix B.

## Chapter 2

### Electrical Methods

#### 2.1 The DC Resistivity Method

##### 2.1.1 Introduction

In the direct current (DC) resistivity method, the spatial distribution of the resistivity of the subsurface is investigated. Typically, a four-electrode configuration is used in which the electrical circuit is created by deploying two electrodes and the potential difference is measured between two other electrodes. In electrical studies, electrodes may be placed on the ground and/or in boreholes (Rubin and Hubbard, 2005). The electrical resistivity of a rock sample depends on its mineral content, the amount and structure of its porosity, and the amount and resistivity of the contained fluid in that sample (Parasnis, 1997). Resistivities vary widely from one material to another. For instance, a good conductor such as copper has a resistivity of  $10^{-8}$   $\Omega\text{m}$ , topsoil as an intermediate conductor has a resistivity of 10  $\Omega\text{m}$ , and a bad conductor such as a dry sandstone can have a resistivity of  $10^8$   $\Omega\text{m}$ . Based on this variety in the resistivity of Earth materials, measuring subsurface resistivity has the potential of being very useful in extracting information about subsurface structure (Herman, 2001). There

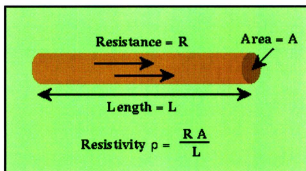


Fig. 2.1: Resistivity vs. resistance (Boyed, 2003).

is a broad range of applications for electrical methods such as prospecting for water-bearing formations, inferring stratigraphic correlations in oil fields, prospecting for conductive ore bodies, detecting fractures and cavities in the subsurface, delineating archaeological features, and environmental applications such as monitoring pollution in the ground (Parasnis, 1997).

### 2.1.2 Resistivity basics

From the physical point of view, the resistivity of a material is defined using an ideal cylinder of length  $L$  and cross-sectional area  $A$  of uniform composition. To express the total resistance ( $R$ ) of the cylinder in terms of its geometrical parameters, resistivity  $\rho$  appears as the mathematically specific constant of proportionality (Fig. 2.1) :

$$R = \rho \frac{L}{A} . \quad (2.1)$$

Also, Ohm's law can be used to obtain the total resistance experimentally:

$$R = \frac{V}{I} , \quad (2.2)$$

where  $V$  is the potential difference between two ends of the cylindrical tube and  $I$  is the total current flowing through it (Fig. 2.2). By combining these two equations,

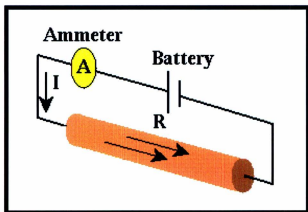


Fig. 2.2: Current flow and Ohm's Law (Boyed, 2003).

the resistivity of the material as its intrinsic property can be expressed as a function of experimentally measured extrinsic resistance:

$$\rho = \left(\frac{V}{I}\right)\left(\frac{A}{L}\right) = R_{app}K \quad (2.3)$$

where  $R_{app}$  is the apparent resistance and  $K$  is a “geometric factor” which in this specific example represents the geometry of the cylinder (Herman, 2001).

### 2.1.3 Potential in homogeneous media

Assume an isotropic homogeneous medium in which a continuous current is flowing. The current passing through  $\delta\mathbf{A}$  is equal to  $\mathbf{J} \cdot \delta\mathbf{A}$  where  $\delta\mathbf{A}$  is a surface element of the medium and  $\mathbf{J}$  is the current density. Ohm's law relates the current density  $\mathbf{J}$  to

the electric field  $\mathbf{E}$  via the equation :

$$\mathbf{J} = \sigma \mathbf{E} \quad (2.4)$$

where  $\sigma$  is the conductivity of the medium in  $S/m$ . The conductivity is the reciprocal of resistivity. Also, in the steady state situation, the electric field can be defined as the gradient of a scalar potential:

$$\mathbf{E} = -\nabla V \quad (2.5)$$

where  $V$  is the potential in Volts. Therefore the current density can be described as

$$\mathbf{J} = -\sigma \nabla V . \quad (2.6)$$

Conservation of charge inside a volume  $R$  surrounded by a closed surface  $A$  that contains no source or sink of current can be expressed by

$$\int_A \mathbf{J} \cdot d\mathbf{A} = 0 . \quad (2.7)$$

Using Gauss' theorem,

$$\int_A \mathbf{J} \cdot d\mathbf{A} = \int_R \nabla \cdot \mathbf{J} = 0 . \quad (2.8)$$

Equation (2.8) is true for any volume  $R$  in the source free area, therefore the integrand can be equated to zero :

$$\nabla \cdot \mathbf{J} = -\nabla \cdot (\sigma \nabla V) = 0 . \quad (2.9)$$

Taking  $\sigma$  as a constant value, the above equation results in Laplace's equation (Telford et al., 1976):

$$\nabla^2 V = 0 . \quad (2.10)$$

Between two uniform media of different conductivities, the following two boundary conditions must be satisfied. Firstly, the potential must be continuous across the boundary from one medium to the next. Secondly, the normal component of  $\mathbf{J}$  must be continuous. The properties of the two media are denoted by subscripts 1 and 2. Hence,

$$V^{(1)} = V^{(2)} \quad , \quad J_n^{(1)} = J_n^{(2)} \quad (2.11)$$

The preceding boundary conditions can be expressed in terms of electric fields :

$$E_t^{(1)} = E_t^{(2)} \quad , \quad \sigma_1 E_n^{(1)} = \sigma_2 E_n^{(2)} \quad (2.12)$$

where “t” and “n” mean tangential and normal components respectively (Telford et al.,1976).

#### 2.1.4 Single current electrode at depth

Consider a point current electrode buried in a homogeneous isotropic medium. Suppose the other current electrode is at infinity (see Fig. 2.3). Based on the spherical symmetry of the system, the potential is a function only of the distance,  $r$ , from the buried electrode. Laplace’s equation in spherical coordinates containing only the  $r$  dependence is:

$$\nabla^2 V = \frac{d^2 V}{dr^2} + \frac{2}{r} \frac{dV}{dr} = 0 \quad (2.13)$$

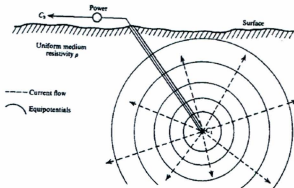


Fig. 2.3: Buried point source of current in homogeneous medium (Telford et al., 1976).

for everywhere except right at the source. Integrating the product of the above equation with  $r^2$  gives (Telford et al., 1976):

$$\frac{dV}{dr} = \frac{A}{r^2} \quad (2.14)$$

where A is a constant of integration. Integrating again results in the following expression for the potential:

$$V = -\frac{A}{r} + B \quad (2.15)$$

where B is a second constant of integration. The usual convention is to take V to be zero at  $r \rightarrow \infty$ . Hence, the constant B must be equal to zero. Since the potential V depends only on r, current is purely radial. Therefore, the total current passing through a complete sphere of radius r centered on the point electrode is given by:

$$I = 4\pi r^2 J = -4\pi r^2 \sigma \frac{dV}{dr} = -4\pi \sigma A. \quad (2.16)$$

So, the constant  $A$  is

$$A = -\frac{I\rho}{4\pi}, \quad (2.17)$$

and finally the potential is given by :

$$V = \frac{I\rho}{4\pi r}. \quad (2.18)$$

As is shown in Fig. 2.3, the equipotentials are spheres centered on the point electrode and hence given by  $r = \text{constant}$ .

### 2.1.5 Single current electrode at the Earth's surface

Assume that the point electrode which introduces the current  $I$  is placed on the surface of a homogeneous isotropic medium (see Fig. 2.4). Again, the other current electrode is assumed to be at infinity. Also, the air is considered to have a zero conductivity. As before,  $B = 0$  as  $V = 0$  when  $r \rightarrow \infty$ . However, in this case all the current flows

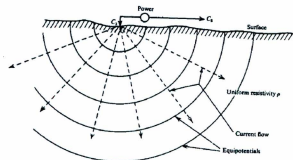


Fig. 2.4: Point source of current at the surface of homogeneous medium (Telford et al., 1976).

through a hemisphere surface (see Fig. 2.4) which means:

$$A = -\frac{I\rho}{2\pi} \quad (2.19)$$

and the potential is:

$$V = \frac{I\rho}{2\pi} \left(\frac{1}{r}\right). \quad (2.20)$$

### 2.1.6 Two current electrodes at the surface

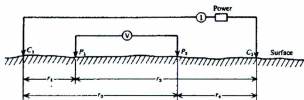


Fig. 2.5: Two current and two potential electrodes on the surface of a homogeneous isotropic ground of resistivity  $\rho$  (Telford et al., 1976).

When both current electrodes are considered on the surface (see Fig. 2.5), the potential anywhere in the subsurface will be affected by both. As before, the potential at  $P_1$  from  $C_1$  is:

$$V_1 = -\frac{A_1}{r_1} \quad \text{where} \quad A_1 = -\frac{I\rho}{2\pi} \quad (2.21)$$

and the potential at  $P_1$  from  $C_2$  is :

$$V_2 = -\frac{A_2}{r_2} \quad \text{where} \quad A_2 = \frac{I\rho}{2\pi} = -A_1 \quad (2.22)$$

$A_1$  and  $A_2$  have a different sign because the current at the two electrodes is equal but in opposite directions. The total potential at  $P_1$  is:

$$V_1 + V_2 = \frac{I\rho}{2\pi} \left( \frac{1}{r_1} - \frac{1}{r_2} \right) \quad (2.23)$$

The difference in potential between the two potential electrodes  $P_1$  and  $P_2$  is :

$$\Delta V = \frac{I\rho}{2\pi} \left\{ \left( \frac{1}{r_1} - \frac{1}{r_2} \right) - \left( \frac{1}{r_3} - \frac{1}{r_4} \right) \right\} \quad (2.24)$$

The current distribution and equipotentials are shown in Fig. 2.6. This four electrode

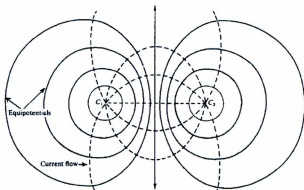


Fig. 2.6: Plan view of equipotentials and current flow-lines for two point sources of current on a homogeneous half-space (Dobrin, 1960).

arrangement represents many layouts usually employed in resistivity work. Some of the most common DC resistivity arrays are shown in Fig. 2.7. Rearranging equation (2.24) gives:

$$\rho = \frac{2\pi\Delta V}{I} \left[ \frac{1}{\left\{ \left( \frac{1}{r_1} - \frac{1}{r_2} \right) - \left( \frac{1}{r_3} - \frac{1}{r_4} \right) \right\}} \right]. \quad (2.25)$$

So the resistivity  $\rho$  of the homogeneous half-space can be computed using the above equation knowing the location of the electrodes, the amount of input current, and the measured voltage. Since the Earth is not a homogeneous medium with a constant resistivity, the computed resistivity will not correspond to the true resistivity of the Earth but will be an average, representative value called the apparent resistivity.

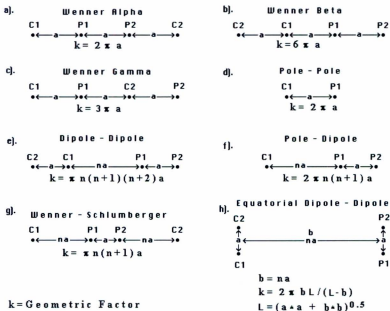


Fig. 2.7: Common arrays used in surface resistivity surveys and their geometric factors (Loke, 1999).

## 2.1.7 Borehole DC resistivity methods

DC resistivity surveys can be employed in a borehole using several array layouts.

Borehole DC improves the resolution of the resistivity method at depth.

### 2.1.7.1 Single borehole survey

The Mise-à-la-masse method is a borehole-based configuration which is common in mineral exploration. In this method, one of the current electrodes is often placed in a borehole at depth right inside the mineralized zone while the other is placed a substantial distance away on the ground surface (see Fig. 2.8). Readings are made

at several sites on the surface using one potential electrode while the other is a remote electrode. For instance, the Geological Survey of Canada conducted several Mise-à-la-masse surveys for ore body delineation including the Victoria graphite deposit in Ontario to correlate high-grade graphite zones between holes, the Hoyle pond gold deposit in Ontario for mapping the orientation of conductive gold bearing alteration zones, and the Stratmat deposit in New Brunswick to resolve the structural relationship between two massive sulphide zones (Mwenifumbo, 1997).

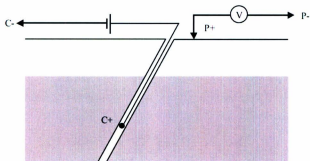


Fig. 2.8: Mise-à-la-masse array (Rubin and Hubbard, 2005).

#### 2.1.7.2 Cross-borehole surveys

The goal in cross-borehole surveys is to produce an image of the resistivity between the boreholes in which the electrodes are installed. Comparing cross-borehole imaging to surface imaging, the main advantages are improved resolution at depth and no need for surface access. Some disadvantages of cross-borehole surveys are that boreholes are of course needed, data sensitivity is constrained to the region between the boreholes, more sophisticated instrumentation is required for data acquisition, and data

processing is more complex. Fig. 2.9 illustrates two examples of cross-borehole config-



Fig. 2.9: Measurement configuration for cross-borehole resistivity imaging. Electrodes A and B are for current injection, M and N are for voltage measurement. Scheme (a) is AM-BN and scheme (b) is AB-MN (Rubin et al., 2005).

urations. In the AM-BN scheme, the two current electrodes are installed in different boreholes as are the potential electrodes. Therefore, the current is injected between two boreholes and the potential difference is also measured between two boreholes. In the AB-MN scheme, current is injected between electrodes in one borehole and the potential difference is measured between potential electrodes in a separate borehole. Because of the dipole length, the AM-BN scheme has a better signal to noise ratio compared to AB-MN scheme (Rubin et al., 2005). The successful imaging of a massive sulphide ore body between boreholes in the Sudbury basin, Ontario by Qian et al. (2007) is an example of the applicability of the cross-borehole configuration in mineral exploration.

## 2.2 The Induced Polarization Method

### 2.2.1 Introduction

In the DC resistivity method with “normal” (i.e., frequency independent) conductivity the voltage is observed as soon as the current is switched on and drops to zero

as soon as the current is switched off (see Fig. 2.10). However, in certain situations

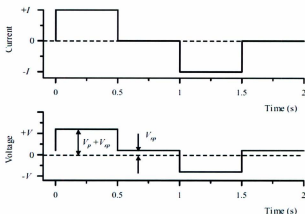


Fig. 2.10: Typical current and idealized voltage wave forms for field DC resistivity surveys.  $V_p$  is the primary voltage and  $V_{sp}$  is observed self-potential voltage (Rubin and Hubbard, 2005).

it is observed that when cutting off the current the voltage does not drop to zero immediately but persists for some time with a continuously decreasing magnitude (see Fig. 2.11). Correspondingly, the voltage between the probes does not reach its maximum value immediately after the current is switched on but instead increases steadily towards the maximum for several seconds or minutes. In geophysical literature, this phenomenon is known as Induced Polarization or IP. This method can be employed in the time domain or the frequency domain. Electronically speaking, the IP effect in the time domain resembles the charging and discharging of a capacitor. In the frequency domain, the IP effect is like the variation of the impedance of a circuit including a resistance and a capacitance in parallel for an alternating current (Parasnis, 1997).

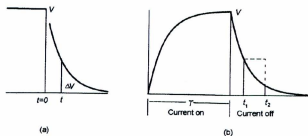


Fig. 2.11: Phenomenon of induced polarization (Parasnis, 1997).

## 2.2.2 Sources of Induced Polarization

In general, there are two main mechanisms that can give rise to IP phenomena: electrode polarization and membrane polarization.

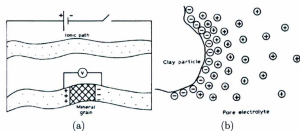


Figure 2.12: (a) Electrode polarization phenomenon at mineral-electrolyte interfaces. (b) Membrane polarization phenomenon in clays (Sharma, 1997).

### 2.2.2.1 Electrode Polarization

In the ground, ions in the electrolytes present in the pores of rocks are predominantly responsible for carrying the electric current. Obstruction of the passage of these ions by certain mineral particles such as common metals that transport the current by electrons, leads to accumulation of the ionic charges at the interface of the particle

and electrolyte (see Fig. 2.12 a). The positive charges accumulate at the surface where current enters the particle and negative charges accumulate where the current leaves. The appearance of separate concentrations of positive and negative charge is called polarization. Once the current is switched off the ions slowly diffuse back into the pore electrolyte. This process is also observed during ordinary electrolysis, at the surface of metal electrodes dipped in an electrolyte. Physical chemists have been familiar with this phenomenon for a long time and have referred to it as the over-voltage effect. Foremost among the ore minerals that have an electronic mode of conduction and therefore can exhibit strong IP effects are pyrite, pyrrhotite, chalcopyrite, graphite, galena, bornite, magnetite and pyrolusite (Sharma, 1997).

#### **2.2.2.2 Membrane Polarization**

Membrane polarization must be evoked for explaining the IP effects that are observed even when no metallic type minerals are present in the ground. It mostly owes its origin to the presence of clay particles that tend to have negative surface charges. Existence of the clay particles with negatively charged surfaces results in attraction of positive ions from the electrolyte in the capillaries of a clay aggregate. Therefore, an electrical double layer is formed at the surface of the clay particles (see Fig. 2.12 b). The positive ions accumulated on the clay particles will be displaced by the flow of a macroscopic electric current. An IP effect is the result of the process of charge redistribution that manifests itself as a decaying voltage. Once the current is terminated, the positive ions will diffuse back to their equilibrium arrangement

(Sharma, 1997).

### 2.2.3 Measuring the IP Effect in Time Domain

As mentioned at the end of section 2.2.1, the IP effect can be measured in the time domain and the frequency domain. The same four-electrode configurations as used for DC resistivity are typically employed for surface IP surveys.

#### 2.2.3.1 Polarizability

If the IP survey is conducted using DC pulses of duration  $T$  and the reading is made by measuring the voltage  $\Delta V$  remaining at a certain time  $t$  after current cut-off, the observed IP magnitude is usually expressed as (see Fig. 2.11):

$$\eta = \frac{\Delta V}{V} \quad (2.26)$$

where  $V$  is the maximum voltage that was measured while the current was on. This quantity is known as “polarizability”, and is typically quoted in units of  $\frac{mV}{V}$ . If  $\Delta V$  and  $V$  have been measured in the same physical unit (Volts or milliVolts), the IP effect can be expressed as a percentage, i.e.,  $100(\frac{\Delta V}{V})$ . In IP surveys,  $T$  is usually chosen to be in the range of 1 – 20s. The time  $t$ , which is a fraction of  $T$ , must be chosen carefully since it must be long enough for EM induction effects to have disappeared but short enough for  $\Delta V$  to be in the sensitivity of the detecting device (Parasnis, 1997).

### 2.2.3.2 Chargeability

Chargeability is defined as the normalized time integral representing the area under the voltage decay curve between two times after interrupting the current (see Fig. 2.11 b). Specifically :

$$M_{t_1, t_2}^T = \left(\frac{1}{V}\right) \int_{t_1}^{t_2} \Delta V_{IP} dt \quad (2.27)$$

where  $t_1$  and  $t_2$  are the specific time after current cut off,  $V$  is the maximum voltage that was measured while the current was on and  $\Delta V_{IP}$  is the potential variation function while the current is off. The unit of chargeability is ( $mVsV^{-1}$ ) in which  $\Delta V$  and  $V$  are measured in millivolts and Volts respectively and time is in second. In some literature, “polarizability” is also called “chargeability” but because of the difference in physical unit, it is better to use two different terms for them (Parasnis, 1997).

## 2.2.4 Measuring the IP Effect in Frequency Domain

### 2.2.4.1 Percentage frequency effect, PFE

In a frequency-domain IP survey, the apparent resistivity of the Earth is determined by any kind of electrode configuration at two frequencies,  $F$  and  $f$  ( $F > f$ ). In this method, IP measurement is expressed as the frequency effect:

$$(FE_{F,f}) = \frac{\rho_a(f) - \rho_a(F)}{\rho_a(f)} \quad (2.28)$$

where  $\rho_a(f)$  and  $\rho_a(F)$  are the measured apparent resistivities in two different frequencies  $f$  and  $F$  respectively. If the above quantity is expressed as a percentage

in  $\rho_a$ , the IP effect is called “percentage frequency effect ” or PFE (Parasnis, 1997). The common frequency range used in this type of survey is 0.05 – 0.5 Hz for  $f$  and 1 – 10 Hz for  $F$  (Sumner, 1976).

#### 2.2.4.2 Metal Factor

Metal factor is another frequency-domain measure of IP which is defined as frequency effect divided by the apparent resistivity at high frequency ( $F$ ):

$$(MF_{F,f}) = \frac{\rho_a(f) - \rho_a(F)}{\rho_a(F)\rho_a(f)}. \quad (2.29)$$

By a simple rearrangement of equation (2.29), metal factor can be written as:

$$(MF_{F,f}) = \sigma_a(F) - \sigma_a(f) \quad (2.30)$$

where  $\sigma_a(F)$  and  $\sigma_a(f)$  are the apparent conductivities at the two frequencies in S/m (Parasnis, 1997).

#### 2.2.4.3 Phase Shift

Phase shift,  $\phi$ , is another IP effect measured in the frequency domain and is defined as the phase difference between the voltage measured by potential electrodes MN and the current introduced into the ground (Parasnis, 1997).  $\phi$  is usually expressed in milliradians, because it has very small values. For instance, its maximum value at a frequency of 1 Hz is usually a few hundredths to one tenth of a radian. In this type of survey, the voltage difference in MN is also measured to provide the apparent resistivity.

### 2.2.5 Borehole IP Methods

Surface IP measurements have some deficiencies such as a lack of depth penetration when conductive overburden is present and decreasing resolution with depth. Borehole IP has been introduced to compensate for these limitations of conventional surface IP surveys. Going from surface to borehole measurements introduces differences both in theory and practice. For instance, in computing the resistivity from subsurface measurements the geometric factor is two times that used for surface measurements, since the equipotentials in the subsurface are spheres rather than the hemispheres for the surface investigations (see Sections 2.1.4 and 2.1.5) (Sumner, 1976).

#### 2.2.5.1 Classical Borehole IP

The traditional borehole method where one of the current electrodes is in one borehole, uses the fact that as the separation between current electrodes is increased, measurements are sensitive to regions further from the borehole axis. The lateral distribution of electrical properties of the geological formation such as chargeability and resistivity can be studied by measuring the voltages as a function of electrode separation. Two types of devices are employed in this kind of survey, normal probe and lateral probe (see Fig. 2.13). As illustrated in Fig. 2.13(a), a normal probe comprises one current electrode and one voltage electrode separated by a distance  $L$  which is called probe length. Both the return current electrode,  $B$ , and the voltage reference electrode,  $N$ , are grounded far from the probe on the Earth's surface. The separation between

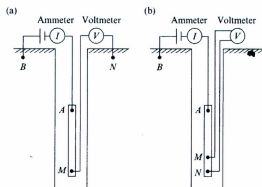


Fig. 2.13: (a) Normal and (b) lateral probes used in classical borehole IP (Kaufman and Anderson, 2010).

electrodes B and N is much greater than the probe length. The lateral probe (see Fig. 2.13 b) includes two potential electrodes, M and N, and one current electrode, A. The separation between the two potential electrodes is much smaller than the distance to the electrode A (*i.e.*,  $MN \ll AM$ ). In the case of the lateral probe, the probe length is equal to the distance from A to the midpoint of MN. Like the normal probe, the return current electrode (B) is installed far away from the borehole. Similar to the surface survey, both DC resistivity and IP measurements can be made using these two probe configurations. The lateral probe is the most common array used for borehole IP surveys (Kaufman and Anderson, 2010).

#### 2.2.5.2 Hole-to-hole IP survey

Just like borehole DC resistivity, classical borehole IP using the normal or lateral probe configuration has several limitations such as investigation range restricted by

borehole depth, limited depth of measurement, and sensitivity to in-hole mineralization, 3D inversion is not always effective. In this thesis, I investigate a novel IP borehole survey design through numerical modeling and inversion. The new survey design, which was introduced by Abitibi Geophysics, is called hole-to-hole IP. In this configuration, the current electrodes are placed on the Earth's surface with a separation at least two times the target depth and the potential electrodes are deployed in two separate boreholes (see Fig. 2.14) (Berube, 2010). Measurements are typically made every 5 to 25 meters down the boreholes. Based on the surveys that have been

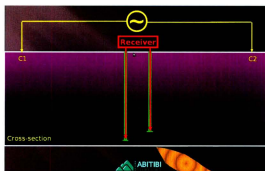


Fig. 2.14: Hole-to-hole IP array, (Berube, 2010).

done to date by Abitibi Geophysics using this method, the hole-to-hole arrangement has the following advantages compared to the classical borehole IP: measured data are suitable for robust 3D inversion, depth of investigation can be greater than 460 m, geological noise is less, the cost is the same as classical IP, and neither special cables nor costly probes are needed (Berube, 2010).

## Chapter 3

### 3D Forward Modelling and Inversion of IP - Theory

#### 3.1 3D Forward modelling of IP data

In a typical DC/IP survey, current  $I$  is injected into the ground and the resulting potential is measured at various locations away from the source which could be either on the surface or down a borehole. In the time domain, the current alternates in direction and the IP voltages are measured in the off-times between the current pulses (see Fig. 2.10). A typical IP time domain effect is illustrated in Fig 3.1. Regarding Fig 3.1,  $\phi_\sigma$  is the potential which would be measured in the absence of a chargeability effect. The relationship between  $\phi_\sigma$  and the electrical conductivity  $\sigma$  is:

$$\phi_\sigma = F_{dc}[\sigma] \quad (3.1)$$

where  $F_{dc}$  denotes the solution of the DC equation (see equation 2.9):

$$\nabla \cdot (\sigma \nabla \phi_\sigma) = -I\delta(r - r_s) \quad (3.2)$$

where  $\sigma$  is the electrical conductivity,  $I$  is the input current,  $r_s$  is the location of the current source and  $\delta$  is the delta Dirac function. Appropriate boundary conditions must be applied to eq. (3.2) (see equations 2.11 and 2.12). The potential  $\phi_\sigma$  calculated in eq. (3.2) is the potential due to a single current. For electrode configurations that

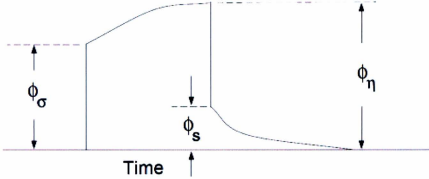


Fig. 3.1: IP effect in Time domain (DCIP3D Manual, UBC-GIF).

include more than one current electrode, the potential can be computed from eq. (3.2) using the principle of superposition.

When the Earth materials are chargeable, the measured voltage will change with time as is shown in Figure 3.1 and reach a maximum value of  $\phi_\eta$ . Chargeability,  $\eta$ , is a dimensionless, positive parameter whose value is limited in the interval  $[0, 1)$ . Siegel (1959) stated that the DC resistivity forward modeling function  $F_{dc}$  can be used to calculate  $\phi_\eta$  by replacing the conductivity  $\sigma$  with  $\sigma(1 - \eta)$ . So,

$$\phi_\eta = F_{dc}[\sigma(1 - \eta)] \quad (3.3)$$

or

$$\nabla \cdot (\sigma(1 - \eta)\nabla\phi_\eta) = -I\delta(r - r_s) . \quad (3.4)$$

Another potential which can be measured as the IP datum is the secondary potential which is :

$$\phi_s = \phi_\eta - \phi_\sigma = F_{dc}[\sigma(1 - \eta)] - F_{dc}[\sigma] . \quad (3.5)$$

The apparent chargeability in the context of forward modelling is defined as:

$$\eta_a = \frac{\phi_s}{\phi_\eta} = \frac{F_{dc}[\sigma(1-\eta)] - F_{dc}[\sigma]}{F_{dc}[\sigma(1-\eta)]}. \quad (3.6)$$

In the UBC package for DC/IP 3D modelling and inversion (DCIP3D), which is the software that is used here, the forward solutions for the DC and IP data are computed by solving eqs. (3.2) and (3.4) for  $\phi_\eta$  and  $\phi_\sigma$  using a finite volume method. The finite volume method uses a rectilinear mesh to specify conductivity,  $\sigma$ , and chargeability,  $\eta$ , for each cell that can be different from one cell to the next. Also, homogeneous boundary conditions are applied on the potential,  $\phi$ , to approximate boundary conditions at infinity (Dey and Morrison, 1979).

### 3.2 3D Inversion of IP data

The DCIP3D program performs two inversion problems. Firstly, the DC potential,  $\phi_\sigma$ , is inverted to recover the electrical conductivity  $\sigma(x, y, z)$ . This is a nonlinear inverse problem. Secondly, the IP data are inverted to recover the chargeability  $\eta(x, y, z)$ . For small values of “ $\eta$ ” the IP inversion problem can be turned into a linear problem with some approximations. To describe the inverse problem, it is convenient to introduce notation for the “data” and the “model”. Having  $N$  as the number of data points the vector  $\mathbf{d} = (d_1, d_2, \dots, d_N)$  denotes the data vector where  $d_i$  could be the  $i^{\text{th}}$  potential in a DC resistivity data-set or the  $i^{\text{th}}$  secondary potential or apparent chargeability in an IP data-set. The symbol  $\mathbf{m}$  is used to describe the physical property that we are interested in. So,  $m_i$  could be the conductivity or chargeability for the  $i^{\text{th}}$

cell. In DCIP3D,  $m_i$  has been chosen to be  $m_i = \ln(\sigma_i)$ , because of the positivity issue and natural range of  $\sigma$ , while inverting for conductivities and  $m_i = \eta_i$  for recovering the chargeability distribution. Appropriate reproduction of the observed data  $\mathbf{d}^{\text{obs}} = (d_1^{\text{obs}}, d_2^{\text{obs}}, \dots, d_N^{\text{obs}})$  is the main purpose of inversion which is achieved by recovering a suitable model vector  $\mathbf{m} = (m_1, m_2, \dots, m_M)$  where  $M$  is the number of cells. Noise in the observed data can lead to artifacts in the model. So, the objective in the inversion is neither to underfit nor overfit the data. To reach this goal a data misfit criterion is introduced:

$$\psi_d = \|\mathbf{W}_d(\mathbf{d} - \mathbf{d}^{\text{obs}})\|^2 \quad (3.7)$$

where  $\mathbf{W}_d$  is a datum weighting matrix and  $\mathbf{d}$  is the data computed by the forward modelling. By considering the noise in the  $j^{\text{th}}$  observation to be uncorrelated Gaussian random noise having zero mean and standard deviation of  $\epsilon_j$ , the appropriate form for  $\mathbf{W}_d$  is the  $N \times N$  diagonal matrix as:

$$\mathbf{W}_d = \text{diag} \left\{ \frac{1}{\epsilon_1}, \dots, \frac{1}{\epsilon_N} \right\}. \quad (3.8)$$

Choosing  $\mathbf{W}_d$  as above,  $\psi_d$  is a random variable with a chi-squared distribution and  $N$  degrees of freedom. So, the expected value for  $\psi_d$  will be approximately equal to  $N$ . This means  $\psi_d^*$ , the target misfit for an inversion, should be close to this value. The inverse problem is mathematically non-unique because the number of cells,  $M$ , is greater than the number data,  $N$ , in order to allow the maximum flexibility to produce a model with arbitrary variation. Also the inverse problem is fundamentally non-unique because of noise in the observations and poor resolution of the physics

of the DC and IP methods. This non-uniqueness is the main problem when trying to obtain unambiguous information about Earth structure from the observations. In other words, there are infinitely many models that can adequately reproduce the observations. The job of a geophysicist is to introduce an appropriate approach to make the inversion algorithm produce a geologically reasonable model. This goal is achieved by incorporating a model objective function in a way that, when minimized, a model with desirable characteristics is produced. In DCIP3D, the model objective function is designed to find a model which has a minimum amount of structure in the vertical and horizontal directions and at the same time is close to a reference model  $\mathbf{m}_0$ . To implement this, a discretized form of the following equation is minimized:

$$\psi_m(m, m_0) = \alpha_s \int \int w_s (m - m_0)^2 dv + \alpha_x \int \int w_x \left( \frac{\partial(m - m_0)}{\partial x} \right)^2 dv + \alpha_y \int \int w_y \left( \frac{\partial(m - m_0)}{\partial y} \right)^2 dv + \alpha_z \int \int w_z \left( \frac{\partial(m - m_0)}{\partial z} \right)^2 dv \quad (3.9)$$

where the spatially dependent weights  $w_s$ ,  $w_x$ ,  $w_y$  and  $w_z$  are specified by the user. The constant  $\alpha_s$  controls the importance of the closeness of the constructed model to the reference model  $\mathbf{m}_0$ . The roughness of the model in three dimensions is controlled by  $\alpha_x$ ,  $\alpha_y$  and  $\alpha_z$ . As an alternative, length scales  $L_x = \sqrt{\frac{\alpha_x}{\alpha_s}}$ ,  $L_y = \sqrt{\frac{\alpha_y}{\alpha_s}}$  and  $L_z = \sqrt{\frac{\alpha_z}{\alpha_s}}$  are sometimes used. The greater the length scale in each direction, the smoother the constructed model in that direction. To have a reasonably smooth model, the length scale should be greater or equal to two cell widths and smaller than the respective dimension of the model region (DCIP3D manual, UBC-GIF). The discrete form of

the eq. (3.9) is :

$$\begin{aligned}\psi_m &= (\mathbf{m} - \mathbf{m}_0)^T \{ \alpha_s \mathbf{W}_s^T \mathbf{W}_s + \alpha_x \mathbf{W}_x^T \mathbf{W}_x + \alpha_y \mathbf{W}_y^T \mathbf{W}_y + \alpha_z \mathbf{W}_z^T \mathbf{W}_z \} (\mathbf{m} - \mathbf{m}_0) \\ &\equiv (\mathbf{m} - \mathbf{m}_0)^T \mathbf{W}_m^T \mathbf{W}_m (\mathbf{m} - \mathbf{m}_0)\end{aligned}\quad (3.10)$$

where the matrices  $\mathbf{W}_s$ ,  $\mathbf{W}_x$ ,  $\mathbf{W}_y$  and  $\mathbf{W}_z$  are produced by finite difference approximation of the spatial derivatives in equation (3.9). Finally, the inverse problem becomes the following optimization problem :

$$\begin{aligned}\text{minimize} & \quad \psi_d + \mu \psi_m \\ \text{subject to} & \quad \psi_d = \psi_d^*\end{aligned}\quad (3.11)$$

where  $\mu$  is the trade-off parameter that is automatically adjusted such that  $\psi_d \approx \psi_d^*$ .

### 3.2.1 Inversion of DC resistivity data: Gauss-Newton Method

DC inversion is a nonlinear problem as the data do not depend linearly on the conductivity model. DCINV3D, part of the DCIP3D package, solves this problem by using the Gauss-Newton approach in which the objective function is linearized about a current model  $\mathbf{m}^{(n)}$ , and a model perturbation is solved for and used to update the current model. Substituting  $\mathbf{m}^{(n+1)} = \mathbf{m}^{(n)} + \delta\mathbf{m}$  into the objective function in equation (3.11):

$$\psi(\mathbf{m} + \delta\mathbf{m}) = \|\mathbf{W}_d(\mathbf{d}^{(n)} + \mathbf{J}\delta\mathbf{m} - \mathbf{d}^{\text{obs}})\|^2 + \mu\|\mathbf{W}_m(\mathbf{m} + \delta\mathbf{m} - \mathbf{m}_0)\|^2 + \text{HOT} \quad (3.12)$$

where HOT represents the Higher Order Terms and  $\mathbf{J}$  is the sensitivity matrix whose element  $J_{ij}$  quantifies the influence of the model change in the  $j^{\text{th}}$  cell on the  $i^{\text{th}}$

datum:

$$J_{ij} = \frac{\partial d_i}{\partial m_j}. \quad (3.13)$$

Setting the higher order terms to zero in equation (3.12) the derivative with respect to  $\delta \mathbf{m}$  yields:

$$(\mathbf{J}^T \mathbf{J} + \mu \mathbf{W}_m^T \mathbf{W}_m) \delta \mathbf{m} = -\mathbf{J}^T (\mathbf{d}^{(n)} - \mathbf{d}^{obs}) - \mu \mathbf{W}_m^T \mathbf{W}_m (\mathbf{m}^{(n)} - \mathbf{m}_0). \quad (3.14)$$

In the above equation, the matrix  $\mathbf{W}_d$  has been absorbed into the sensitivity matrix. This is the main equation to be solved to obtain the model perturbation. The new model is generated by:

$$\mathbf{m}^{(n+1)} = \mathbf{m}^{(n)} + \alpha \delta \mathbf{m} \quad (3.15)$$

where  $\alpha$  is a constant in the interval  $(0, 1]$  which limits the stepsize and is chosen to ensure that the total objective function is reduced (Li and Oldenburg, 2000).

### 3.2.2 IP Inversion

The first step to invert IP data is to linearize equation (3.3). Considering  $\eta_i$  and  $\sigma_i$  as the chargeability and electrical conductivity of the  $i^{\text{th}}$  cell,  $\phi_\eta$  can be linearized about the conductivity model as follows (DCIP3D manual, UBC-GIF):

$$\phi_\eta = \phi(\sigma - \eta\sigma) = \phi(\sigma) - \sum_{j=1}^M \frac{\partial \phi}{\partial \sigma_j} \eta_j \sigma_j + H.O.T. \quad (3.16)$$

Substituting the linearized form of  $\phi_\eta$  into equation (3.3) yields:

$$\phi_s = \phi_\eta - \phi_\sigma = - \sum_{j=1}^M \frac{\partial \phi}{\partial \sigma_j} \eta_j \sigma_j + H.O.T \quad (3.17)$$

which can be approximately written as:

$$\phi_s = - \sum_{j=1}^M \sigma_j \frac{\partial \phi}{\partial \sigma_j} \eta_j = - \sum_j \frac{\partial \phi}{\partial \ln(\sigma_j)} \eta_j . \quad (3.18)$$

If one is working with apparent chargeability as the IP data, substituting the above equation into equation (3.6) yields:

$$\eta_a = - \sum_j \frac{\sigma_j}{\phi_i} \frac{\partial \phi_i}{\partial \sigma_j} \eta_j = - \sum_j \frac{\partial \ln(\phi)}{\partial \ln(\sigma_j)} \eta_j . \quad (3.19)$$

In both cases, either the secondary potential or the apparent chargeability as the  $i^{\text{th}}$  datum is expressed as:

$$d_i = \sum_{j=1}^M J_{ij} \eta_j \quad (3.20)$$

where the sensitivity matrix,  $\mathbf{J}$ , for the secondary potential data ( $d = \phi_s$ ) is :

$$- \frac{\partial \phi_i[\sigma]}{\partial \ln(\sigma_j)} \quad (3.21)$$

and for the apparent chargeability data ( $d = \eta_a$ )  $\mathbf{J}$  is:

$$- \frac{\partial \ln(\phi_i)[\sigma]}{\partial \ln(\sigma_j)} . \quad (3.22)$$

So, in the case of IP, the inversion problem is formulated as :

$$\begin{aligned} \text{minimize} \quad & \psi_m = \|\mathbf{W}_m(\eta - \eta_0)\|^2 \\ \text{subject to} \quad & \|\mathbf{W}_d(\mathbf{J}\eta - \mathbf{d})\|^2 = \psi_d^* \\ & \eta \geq 0 \end{aligned}$$

where  $\psi_d^*$  is a target misfit. To solve the linear inverse problem with positivity constraints, the efficient way is to use a logarithmic barrier method, in which the minimization is performed by a sequence of minimizations that include a logarithmic term

to ensure that each iteration generates a positive model. Therefore, the new objective function is given by:

$$\phi(\lambda) = \phi_d + \mu\phi_m - 2\lambda \left[ \sum_{j=1}^M \ln\left(\frac{\eta_j}{u}\right) + \sum_{j=1}^M \ln\left(1 - \frac{\eta_j}{u}\right) \right], \quad (3.23)$$

where  $\lambda$  is the barrier parameter and  $u$  is an upper bound on chargeability model which could be the theoretical bound of 1.0 or the maximum value of chargeability to be expected from the given data set (Li and Oldenburg, 2000).

## Chapter 4

### Survey design for hole-to-hole IP data - modelling and inversion study

In this chapter, the 3D inversion of hole-to-hole IP data is illustrated for different synthetic Earth models using DCIP3D. The aim is to determine how few (or how many) electrode locations are required to obtain good inversion results, in particular, and how the inversion of hole-to-hole data depends on the number and configuration of electrode locations in general. Therefore, different aspects of both inversion and data set have been investigated to obtain the economically optimum survey design including the minimum number of boreholes and receiver locations for a successful imaging of a chargeable ore body in a mineral exploration project. Finally, the inversion results of hole-to-hole IP field data are presented.

#### 4.1 3D mesh design

The first step in any kind of geophysical forward modelling and inversion is discretizing the Earth model through designing a suitable mesh. There are different kinds of meshes employed for geophysical data modelling. One of the most popular is the rectangular finite difference mesh in which the cells are rectangular prisms with different

aspect ratios. The physical property is assumed to be constant within a cell, and can vary from one cell to the next. MeshTools3D is the software provided by UBC-GIF to design and view 3D models which are represented by rectangular meshes. Here, I am using MeshTools3D to design a 3D mesh for numerical modelling of DC resistivity and IP data as well as illustrating 3D models of the Earth's physical properties that are generated by the program DCIP3D. DCIP3D is a package provided by the UBC-GIF for three dimensional forward modelling and inversion of DC resistivity and IP data. The mesh is divided into two main regions, the core portion which represents the region of interest and the padding zones which ensure that the boundary conditions in the finite difference modelling are handled correctly. Two important factors, namely, the grid on the surface of observation locations and the locations of boreholes, control the horizontal mesh when designing the core portion. To define the maximum depth of the mesh the following two parameters must be considered: depth of investigation and the depth of the deepest borehole electrode. After designing the core region, the mesh should be extended in all directions by a set of padding cells. The boundary conditions are sufficiently handled by using five or more cells whose widths continuously increase outward by a factor of between 1.3 to 2.

#### 4.2 Example 1: Single Chargeable body

The first example model that I consider here is a ( $150m \times 200m \times 300m$ ) cuboidal body that extends from 1175 to 1325 m in the x-direction, from 250 to 450 m in the y-direction and from -400 to -700 m in the z-direction (see Figs. 4.1 and 4.2). This

chargeable body, with chargeability of 100 mV/V, is embedded in a half-space of zero chargeability. The resistivity of the body is 1000 Ohm-m. There is no resistivity contrast between the body and the background. The current electrodes are 3200 m away from each other at the locations  $(-300,225,0)$  and  $(2900,225,0)$ . The body of interest is almost located in the middle with drill holes all around. Figure 4.2 is a plan view which demonstrates the locations of the drill holes related to the body. Although a made-up chargeable zone is being considered, the borehole locations are taken from a real survey.

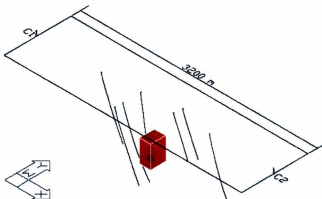


Fig. 4.1: Oblique 3D view of all drill holes, current electrodes and the chargeable body for the first example model.

#### 4.2.1 Mesh design and forward modelling accuracy test

The mesh should be designed in a way that is sufficiently fine in the core region and has boundaries sufficiently far away that the numerical modelling is sufficiently accurate, but the number of cells is small enough that the programs can fit into available

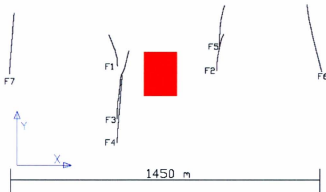


Fig. 4.2: Plan view of the 7 drillholes and chargeable body.

computer memory. I designed several meshes, and applied a basic test by comparing DC resistivity and potentials computed using each mesh with the theoretical values. The boundary conditions must be satisfied for the designed mesh, in particular, the padding zone must extend far enough so that the potential tends to zero at the edge of the mesh. Another thing which should be considered is the depth of the deepest drill hole, in this case hole  $F_4$  with a depth of 1055.57 m. The model is a half-space with the chargeable body in the middle. This simple geometry allows for an independent analytical solution check on the accuracy of the potentials computed using the mesh. The potential on the surface of this half-space can be calculated using the 4 electrode configuration formula (eq. 2.24). In this example, the locations of the current electrodes are always fixed and the first two locations for the potential electrodes in  $F_1$  and  $F_2$  have been selected. The coordinates of the four electrodes are,  $c_1 = (-300, 225, 0)$ ,  $c_2 = (2900, 225, 0)$ ,  $p_1 = (1053, 285, 0)$  and  $p_2 = (1512, 263, 0)$ . Using equation (2.24) with  $I = 1A$ , the potential difference over the half-space is

equal to  $0.058V$ . This value can be used as a reference for evaluating the quality of the designed mesh. Several meshes were designed and examined by applying the forward modeler over the Earth model in Figures 4.1 and 4.2. Figures 4.3 and 4.4 show the calculated DC potential and chargeability over the Earth model for all designed meshes. Also the running time for the forward modelling program as a function of number of cells in each mesh is illustrated in Figure 4.5. Figure 4.3 shows that the

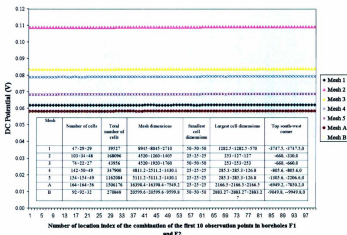


Fig. 4.3: DC potential measurements over the Earth model, Mesh A (blue circles) and Mesh B (red triangles). Other lines correspond to the designed meshes with different dimension and cell size.

last final two meshes which I call Mesh A and Mesh B produced the correct potential ( $0.058V$ ) over the Earth model. Based on the IP graph (see Fig. 4.4), it can be seen that the finer the mesh the more accurate the result will be. Mesh A has a size of  $164 \times 164 \times 56$  cells with a cell size of  $25 \times 25 \times 25$  m in the core portion. Its total number of cells is 1506176 which extends from -6949 to 9449 m in the x-direction,

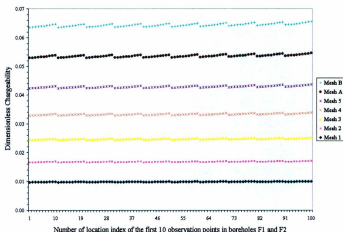


Fig. 4.4: Calculated IP values (dimensionless chargeability) for the Earth model using Mesh A (blue circles) and Mesh B (red triangles).

from -7850 to 8548 m in the y-direction and from 0 to -7549 m in the z-direction (see Figs. 4.6 to 4.9). Mesh B has a size of  $92 \times 92 \times 32$  cells with a cell size of  $50 \times 50 \times 50$  m in the core portion which extends from -9050 to 11550 m in the x-direction, from -9950 to 10650 m in the y-direction and from 0 to -9600 m in the z-direction (see Figs. 4.10 to 4.13). Its total number of cells is 270848. Both meshes have almost the same dimension but Mesh B has the bigger cell size to decrease the running time of the forward program.

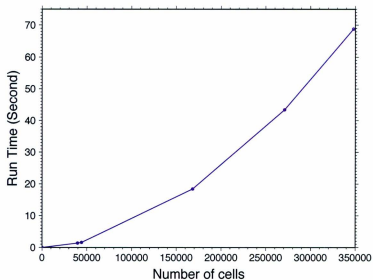


Fig. 4.5: Running time of the forward modelling program DCIPF3D as a function of the number of cells in the mesh.

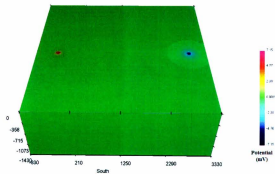


Fig. 4.6: Calculated potential in Volts in Mesh A, 3D view.

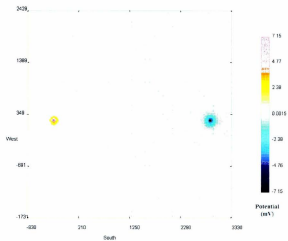


Fig. 4.7: Calculated potential in Volts in Mesh A, plan view.

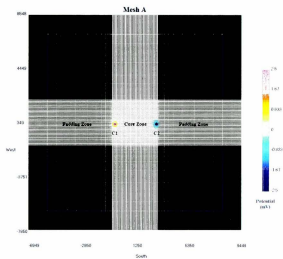


Fig. 4.8: Location of the two current electrodes, Mesh A, showing the cells in the model.

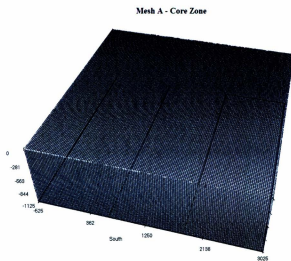


Fig. 4.9: Mesh A, 3D view.

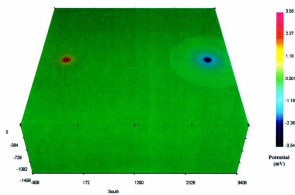


Fig. 4.10: Calculated potential in Volts in Mesh B, 3D view.

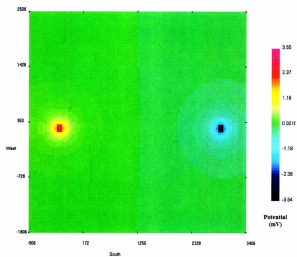


Fig. 4.11: Calculated Potential in Mesh B, plan view.

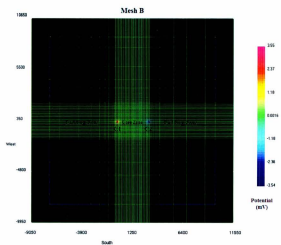


Fig. 4.12: Location of the two current electrodes, Mesh B, showing the cells in the model.

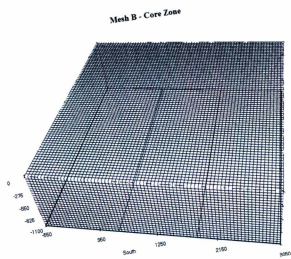


Fig. 4.13: Mesh B, 3D view.

## 4.2.2 Inversion of data from different boreholes combinations

Inversions were done for potentials computed for several combinations of the boreholes and the model illustrated in Fig. 4.2. Gaussian noise with a standard deviation equal to 5% of the average of the calculated DC potential data and calculated IP data was added to the data to produce the synthetic data-sets that were inverted. The results of the inversions for the different combinations of boreholes using both Meshes A and B are represented here. The resistivity model required by the IP inversion is specified as the correct homogeneous half-space.

### 4.2.2.1 Inversion of data from boreholes F1 and F2

The IP sensitivity matrix  $\mathbf{J}$  (eq. 3.13) for boreholes F1 and F2 is illustrated in Fig. 4.14. The locations of the boreholes and the chargeable body are clearly recognizable. The result for Mesh A has better resolution as it has finer cells, but no important difference can be found using the coarse mesh, Mesh B. The constructed chargeability models are illustrated in Figs. 4.15 and 4.16. Boreholes F1 and F2 have depths of 835.85 *m* and 637.02 *m* respectively. The data set was made up of every 10 *m* observation points down the two boreholes, giving a total number of 252 data points, as dimensionless chargeabilities. As shown in Figs. 4.15 and 4.16, the inversion results have a better resolution with finer mesh. The chargeability in the constructed models is always close to the boreholes. Fig. 4.17 shows that for both meshes, synthetic data and predicted data are suitably matched with the final values of misfit of 255.91 and 248.15 for Mesh A and B respectively which are closely enough to the number of data

points (252). Since the results for meshes A and B are so similar, mesh B will be used for the forward modelling to save computational time and memory usage.

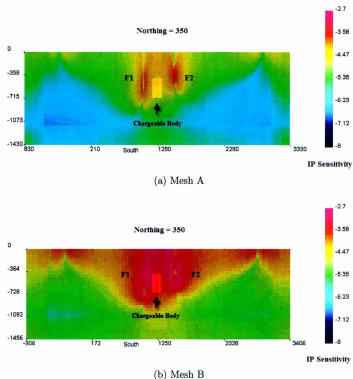


Figure 4.14: IP sensitivity matrix,  $J$ , for boreholes F1 and F2 where the true model is shown via transparency. The color scale represents the cumulative value of sensitivity in each cell.

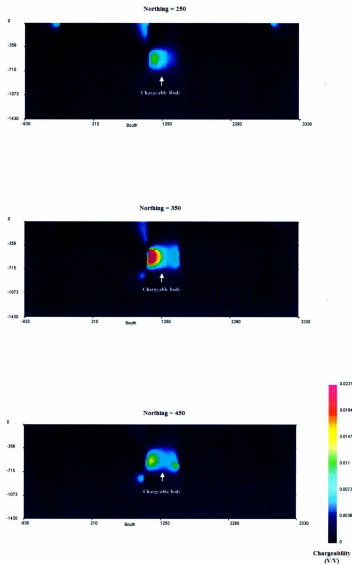


Figure 4.15: Chargeability model constructed of data from boreholes F1 and F2 using mesh A, finer mesh, where the true model is shown via transparency. The color scale represent the values of dimensionless chargeability.

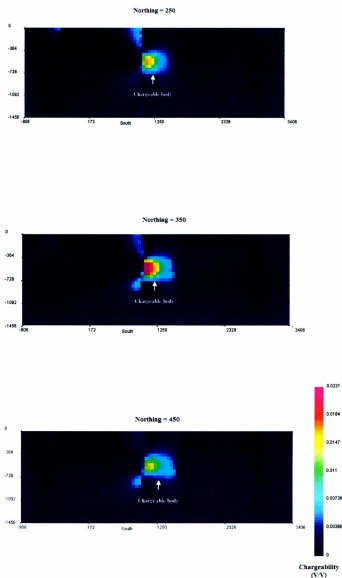
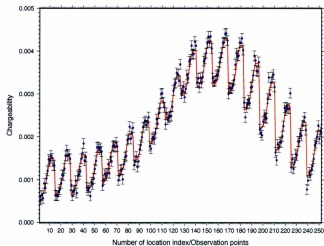
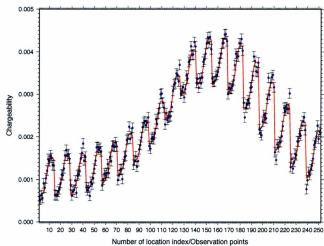


Figure 4.16: Chargeability model constructed from data from boreholes F1 and F2 using mesh B, coarser mesh, where the true model is shown via transparency. The color scale represent the values of dimensionless chargeability.



(a) Mesh A



(b) Mesh B

Figure 4.17: Synthetic observed data (blue dots) and predicted data (red line) for the chargeability model derived from F1-F2 data.

#### 4.2.2.2 Inversion of data from boreholes F1, F2 and F3

The IP sensitivity matrix,  $J$  for boreholes F1, F2 and F3 is illustrated in Fig. 4.18. The locations of all three boreholes and the chargeable body are clearly recognizable. The constructed chargeability model is illustrated in Figs. 4.19 where mesh B has been used to reduce the computation time. Boreholes F1, F2 and F3 have depths of 835.85 m, 637.02 m and 1052.10 m respectively. The data set was produced by observation point every 20 m combining F1 - F2, F1 - F3 and F2 - F3 borehole pairs, with the total number of data of 147, as dimensionless chargeabilities. Fig. 4.20 shows that synthetic data and predicted data are suitably matched. The final value of misfit was 150.15.

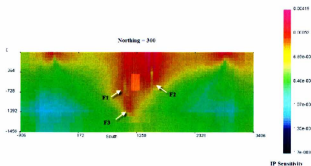


Fig. 4.18: IP sensitivity matrix for boreholes F1, F2 and F3 where the true model is shown via transparency. The color scale represents the cumulative value of sensitivity in each cell.

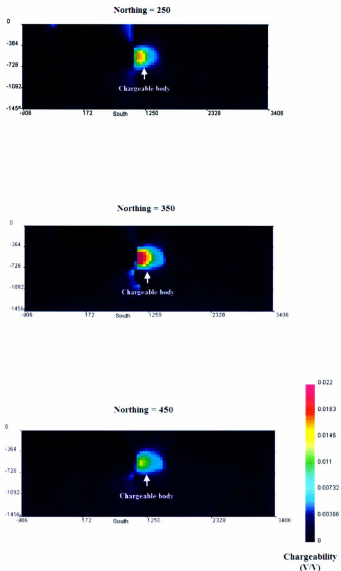


Figure 4.19: Chargeability model constructed from data from boreholes F1, F2 and F3 using mesh B where the true model is shown via transparency. The color scale represent the values of dimensionless chargeability.

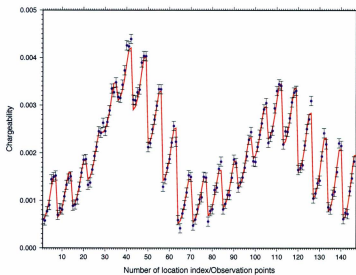


Fig. 4.20: Synthetic observed data (blue) and predicted data (red) for the chargeability model derived from F1, F2 and F3 data.

#### 4.2.2.3 Inversion of data from boreholes F1, F2 and F4

The IP sensitivity matrix for boreholes F1, F2 and F4 is illustrated in Fig. 4.21. The locations of all three boreholes and the chargeable body are clearly recognizable. The constructed chargeability model using Mesh B is illustrated in Fig. 4.22. Boreholes F1, F2 and F4 have depths of 835.85 m, 637.02 m and 1055.57 m respectively. The data set was produced for observation points every 20 m combining F1 - F2, F1 - F4 and F2 - F4 borehole pairs. The total number of data is 147, as dimensionless chargeabilities. Fig. 4.23 shows that the synthetic data and predicted data are suitably matched. The final value of misfit was 150.29.

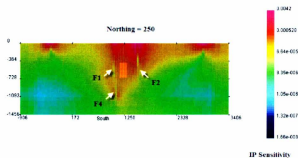


Fig. 4.21: IP sensitivity matrix for boreholes F1, F2 and F4 where the true model is shown via transparency. The color scale represents the cumulative value of sensitivity in each cell.

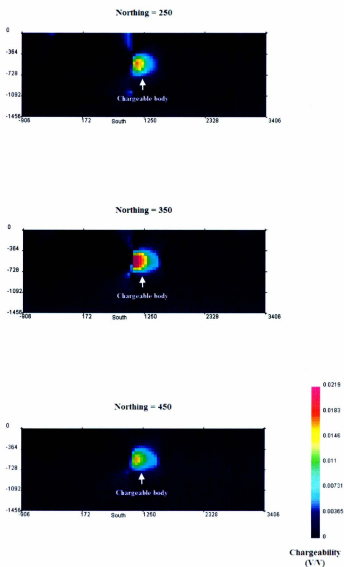


Figure 4.22: Chargeability model constructed for data from boreholes F1, F2 and F4 using mesh B where the true model is shown via transparency. The color scale represent the values of dimensionless chargeability.

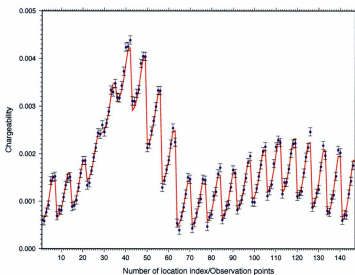


Fig. 4.23: Synthetic observed data (blue) and predicted data (red) for the chargeability model derived from F1, F2 and F4 data.

#### 4.2.2.4 Inversion of data from boreholes F1, F2 and F5

The IP sensitivity matrix for boreholes F1, F2 and F5 is illustrated in Fig. 4.24. The locations of all three boreholes and the chargeable body are clearly recognizable. The chargeability model constructed using Mesh B is illustrated in Fig. 4.25. Boreholes F1, F2 and F5 have depths of 835.85 m, 637.02 m and 673.77 m respectively. The data set was produced for every 20 m observation point combining F1 - F2, F1 - F5 and F2 - F5 borehole pairs, with the total number of data of 126, as dimensionless chargeabilities. Fig. 4.26 shows that for both meshes, synthetic data and predicted data are suitably matched. The final value of misfit was 139.64. The results from 3 hole combinations are summarized in Fig. 27.

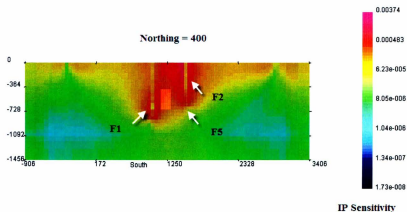


Fig. 4.24: IP sensitivity matrix for boreholes F1, F2 and F5 where the true model is shown via transparency. The color scale represents the cumulative value of sensitivity in each cell.

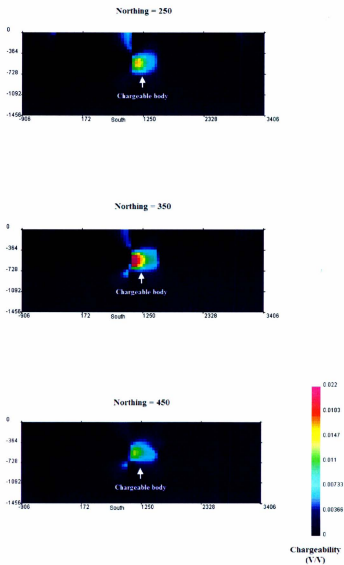


Figure 4.25: Chargeability model constructed from data from boreholes F1, F2 and F5 using mesh B where the true model is shown via transparency. The color scale represent the values of dimensionless chargeability.

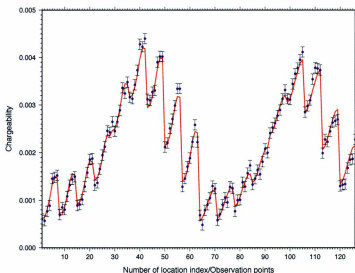


Fig. 4.26: Synthetic observed data (blue) and predicted data (red) for the chargeability model derived from F1, F2 and F5 data.

HOLE COMBINATION	HOLE DEPTH	DIPOLE LENGTH	TOTAL NUMBER OF OBSERVATION POINTS	DATA MISFIT	DATA MISFIT (%)
F1, F2 and F3	853.85, 617.02 and 1052.10 m	20 m	147	150.15	2.14
F1, F2 and F4	853.85, 617.02 and 1055.57 m	20 m	147	150.28	2.14
F1, F2 and F5	853.85, 617.02 and 473.77 m	20 m	126	139.64	10.15

Fig. 4.27: Comparing the results of three hole combination.

#### 4.2.2.5 Inversion of data from boreholes F1, F2, F3, F4 and F5

The IP sensitivity matrix for boreholes F1, F2, F3, F4 and F5 is illustrated in Fig. 4.28. The locations of all boreholes and the chargeable body are clearly recognizable. The constructed chargeability model is illustrated in Figs. 4.29 using mesh B. Boreholes F1, F2, F3, F4 and F5 have depths of 835.85 m, 637.02 m, 1052.10 m, 1055.57 m, and 673.77 m respectively. The data set was produced for every 20 m observation point combining F1 - F2, F1 - F3, F1 - F4, F1 - F5, F2 - F3, F2 - F4, F2 - F5, F3 - F4, F3 - F5, and F4 - F5 borehole pairs, with the total number of data of 486, as dimensionless chargeabilities. Fig. 4.30 shows that for both meshes, synthetic data and predicted data are suitably matched. The final value of misfit was 502.45.

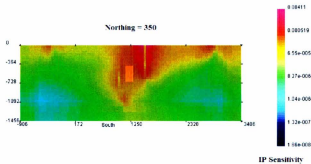


Fig. 4.28: IP sensitivity matrix for boreholes F1, F2, F3, F4 and F5 where the true model is shown via transparency. The color scale represents the cumulative value of sensitivity in each cell.

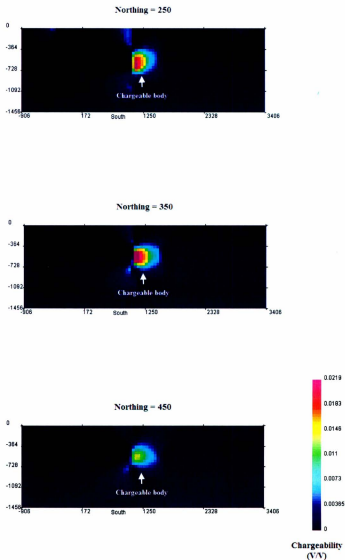


Figure 4.29: Chargeability model constructed of data from boreholes F1, F2, F3, F4 and F5 using mesh B where the true model is shown via transparency. The color scale represent the values of dimensionless chargeability.

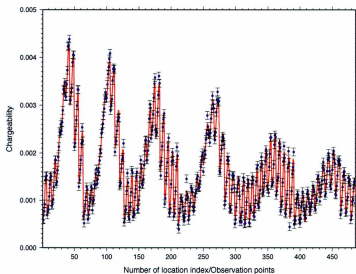


Fig. 4.30: Synthetic observed data (blue) and predicted data (red) for the chargeability model derived from F1, F2, F3, F4 and F5 data

#### 4.2.2.6 Inversion of data from all boreholes

The IP sensitivity matrix for all boreholes is illustrated in Fig. 4.31. The locations of all boreholes and the chargeable body are clearly recognizable. The constructed chargeability model is illustrated in Fig. 4.32. Boreholes F1, F2, F3, F4, F5, F6, and F7 have depths of 835.85 m, 637.02 m, 1052.10 m, 1055.57 m, 673.77 m, 949.44 m, and 960.59 m respectively. The data set was produced for every 20 m observation point combining F1 - F2, F1 - F3, F1 - F4, F1 - F5, F1 - F6, F2 - F3, F2 - F4, F2 - F5, F2 - F7, F3 - F4, F3 - F5, F3 - F5, F3 - F6, F4 - F5, F4 - F6, F4 - F7, F5 - F6, F5 - F7, and F6 - F7 borehole pairs, with the total number of data of 1135, as dimensionless chargeabilities. Fig. 4.33 shows that the synthetic data and predicted data are suitably matched. The final value of misfit was 1141.17.

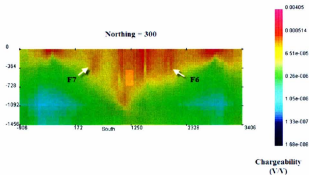


Fig. 4.31: IP sensitivity matrix for all boreholes where the true model is shown via transparency. The color scale represents the cumulative value of sensitivity in each cell.

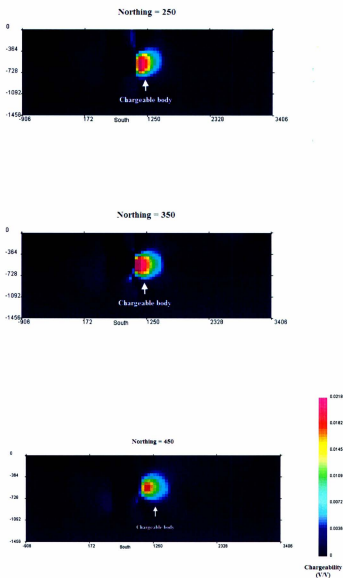


Figure 4.32: Chargeability model constructed of data from all boreholes using mesh B where the true model is shown via transparency. The color scale represent the values of dimensionless chargeability.

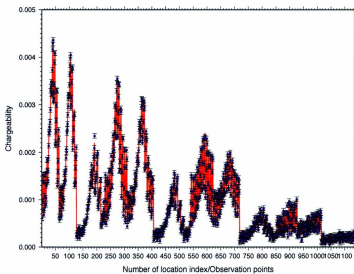


Fig. 4.33: Predicted data (red) and synthetic observed data (blue) for the chargeability model derived for data from all bore holes data.

#### 4.2.2.7 Borehole pairs without anomaly

Inversion were done for the borehole pairs F2 - F6 and F7 - F1. Although the polarisable cube is located outside of these pairs, its effect appears to the correct side of the boreholes. Boreholes F1, F2, F6 and F7 have depths of 835.85 m, 637.02 m, 949.44 m, and 960.59 m respectively. The data set was produced for every 20 m observation point combining F1 - F7 and F2 - F6 borehole pairs, with the total numbers of data of 99 and 77. Since chargeability is the positive quantity and the potentials produced by the chargeable body outside of the boreholes are negative, secondary potentials were used as the IP data for inversion. The final value of misfit was 115.12 and 77.77 for data from boreholes F1 - F7 and F2 - F6 respectively.

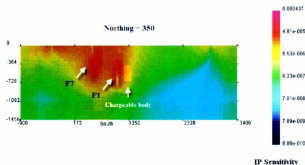


Fig. 4.34: IP sensitivity matrix for boreholes F7 and F1 where the true model is shown via transparency. The color scale represents the cumulative value of sensitivity in each cell.

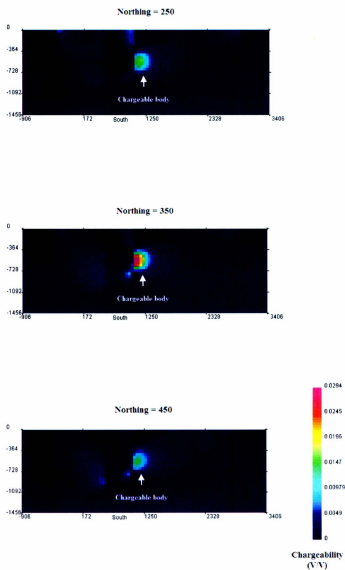


Figure 4.35: Chargeability model constructed from data from boreholes F7 and F1 using mesh B where the true model is shown via transparency. The color scale represent the values of dimensionless chargeability.

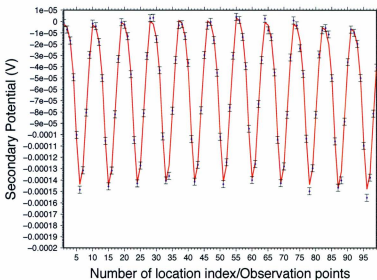


Fig. 4.36: Synthetic observed data (blue) and Predicted data (red) for the chargeability model derived from F7 and F1 data.

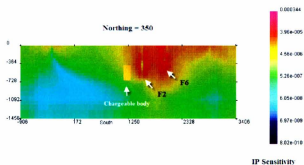


Fig. 4.37: IP sensitivity matrix for boreholes F2 and F6 where the true model is shown via transparency. The color scale represents the cumulative value of sensitivity in each cell.

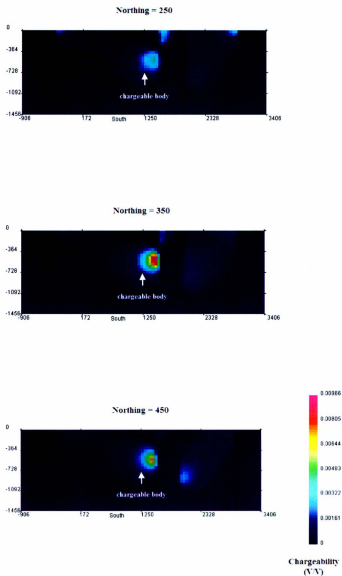


Figure 4.38: Chargeability model constructed of data from boreholes F2 and F6 using mesh B where the true model is shown via transparency. The color scale represent the values of dimensionless chargeability. Final value of misfit was 77.766.

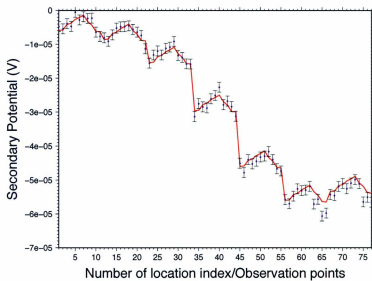


Fig. 4.39: Synthetic observed data (blue) and predicted data (red) for the chargeability model derived from F2 and F6 data.

#### 4.2.2.8 Vertical Borehole pair not straddling the anomaly

To further investigate the behavior of inversion when the chargeable body is not between the measurement boreholes, a synthetic-data set was produced for two parallel vertical boreholes with the causative body placed to the left and right sides of the borehole pair. A target with chargeability of 100 mV/V is embedded in a non-polarisable half-space of conductivity of 0.001 S/m and no resistivity contrast exists. The IP sensitivity matrix for two vertical boreholes for both models are illustrated in Figs. 4.40 and 4.42. The locations of the two vertical boreholes and the chargeable body are clearly recognizable. The constructed chargeability models using Mesh B are illustrated in Figs. 4.41 and 4.43. Results show that the chargeable body in the constructed models appears on the correct side of the boreholes; however, the chargeability in the constructed models remains close to the boreholes than the target. The final values of misfit were 68.136 and 65.282 for the target placed on the right and left sides of the boreholes respectively.

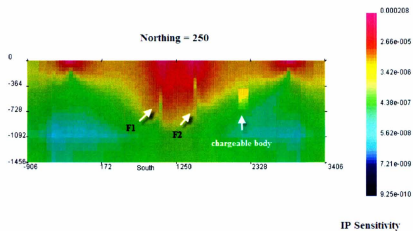


Fig. 4.40: IP sensitivity matrix. Target body is on the right side of the boreholes can be seen because of transparent overlay of true model. The color scale represents the cumulative value of sensitivity in each cell.

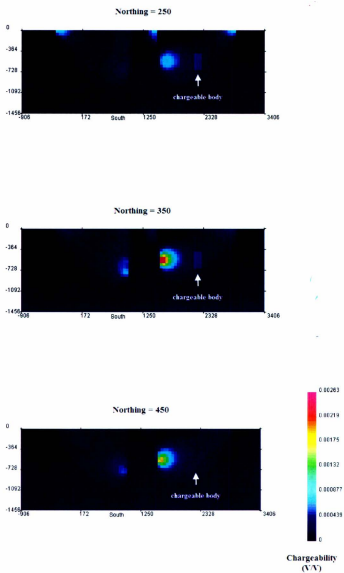


Figure 4.41: Chargeability model constructed from data from vertical boreholes using mesh B. The color scale represent the values of dimensionless chargeability. Target body is on the right side.

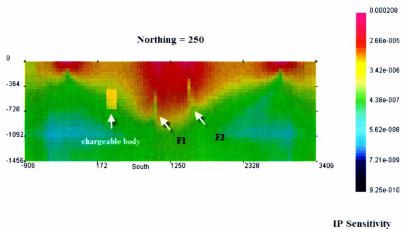


Fig. 4.42: IP sensitivity matrix. Target body is on the left side of the boreholes can be seen because of transparent overlay of true model. The color scale represents the cumulative value of sensitivity in each cell.

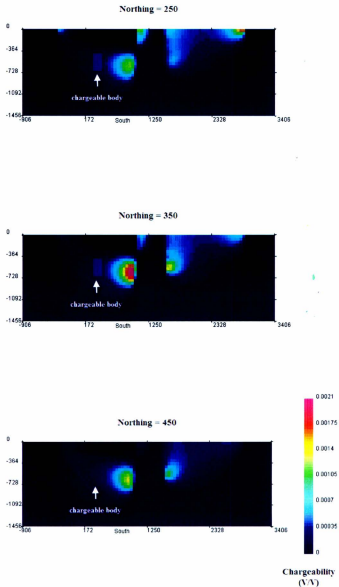


Figure 4.43: Chargeability model constructed from data from vertical boreholes using mesh B. The color scale represents the values of dimensionless chargeability. Final value of misfit was 65.282. Target body is on the left side.

### 4.2.3 Distance weighting function

One characteristic is common to all the inversion results which have been illustrated in the previous sections. The chargeability in the constructed models is concentrated close to the observation locations. This is reminiscent of inversions of gravity and magnetic data. In order to counteract this effect, inversions were tried using a distance weighting. Li and Oldenburg (2000) introduced an effective 3D weighting function for magnetic data-sets that contain borehole measurements in which the sensitivities do not have a predominate decay direction. This weighting function, which is called a distance weighting function, is defined as

$$W_j = \frac{1}{\sqrt{\Delta V_j}} \left\{ \sum_{i=1}^N \left[ \int_{\Delta V_j} \frac{dV}{(R_{ij} + R_0)^\beta} \right]^2 \right\}^{1/4} \quad (4.1)$$

where  $\Delta V_j$  is the volume of  $j$ th cell,  $R_{ij}$  is the distance between the centre of the  $j$ th cell and the  $i$ th observation point, and  $R_0$  is a small constant used to ensure that the integral is well-defined. Usually,  $R_0$  is chosen to be a quarter of the smallest cell dimension. The parameter  $\beta$  for the magnetic and gravity inversions is between  $0.5 \leq \beta \leq 1.5$ . The best value for the parameter  $\beta$  can be found experimentally. Inversions were performed for boreholes F1 and F2 with different values for  $\beta$ . The best value for  $\beta$  for the inversion of hole-to-hole IP data was found to be 0.25 as it pushes the chargeability away from the boreholes in a non-specific, but not in a localized, focused way: see Figs. 4.44 to 4.46.

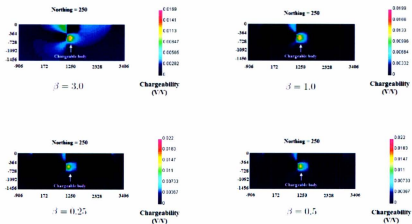


Fig. 4.44: Inversion results using the distance weighting function (Mesh B), F1 and F2, Northing = 250.

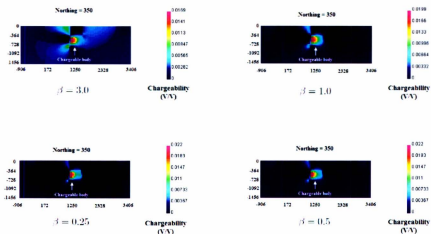


Fig. 4.45: Inversion results using the distance weighting function (Mesh B), F1 and F2, Northing = 350.

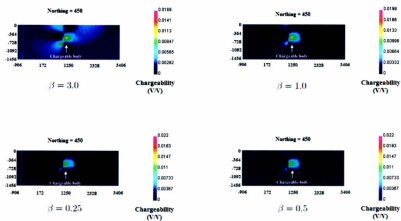


Fig. 4.46: Inversion results using the distance weighting function (Mesh B), F1 and F2, Northing = 450.

### 4.3 Example 2: Aurbel project

#### 4.3.1 Forward modelling

The Earth's synthetic model that I consider for the Aurbel region contains three vertical cuboidal bodies which is described in Fig. 4.47. The chargeable targets are embedded in a half-space of chargeability of 10 mV/V and conductivity of 10000  $\Omega m$ . The current electrodes are at the locations (5332503, 214908, 3300) *m* and (5332259, 216703, 3300) *m*. Figure 4.48 is a plan view which clearly demonstrates the locations of the drill holes. Although made-up chargeable zones are being considered, the borehole locations are taken from a real survey. The constructed chargeability model using Mesh B is illustrated in Fig. 4.49. The data set was produced from twelve pair of boreholes with a total of 1170 data points, as secondary potentials. Fig. 4.50 shows that the synthetic data and predicted data are suitably matched with the final value of misfit of 1165. Although no sign of chargeable bodies A and B can be seen in the constructed models (see Fig. 4.49), their effects are recognizable in both synthetic secondary potentials and predicted data when the inversion was done for the Earth model containing only those chargeable bodies without body C (see Fig. 4.50).

Target	Easting	Northing	Depth	Chargeability	Conductivity
Body A	5332190 to 5332210 m	216150 to 216650 m	3200 to 2600 m	100 mV/V	5000 $\Omega$ m
Body B	5332190 to 5332210 m	215050 to 215550 m	3200 to 2600 m	100 mV/V	5000 $\Omega$ m
Body C	5332490 to 5332510 m	215600 to 216100 m	2600 to 2200 m	100 mV/V	10000 $\Omega$ m

Fig. 4.47: Earth synthetic model information for Aurbel property located east of Val-d'Or, Quebec, Canada.

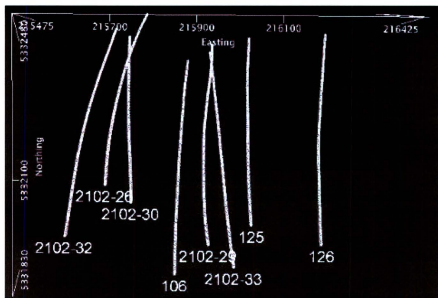
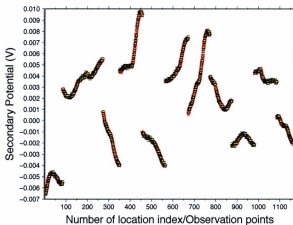
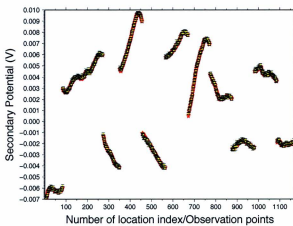


Fig. 4.48: Plan view of the boreholes in Aurbel area.





(a) Earth model containing all three chargeable bodies A, B and C



(b) Earth model containing chargeable bodies A and B

Figure 4.50: Synthetic observed data (yellow) and predicted data (red) for the chargeability model derived from data from all boreholes.

### 4.3.2 Inversion of the field data

Here I present a case history provided by Abitibi Geophysics. The Aurbel property is located east of Val-d'Or covering more than 200 square km of land (see Fig. 4.51). The area of interest (solid red oval, Fig. 4.51) is to the southwest of the Dumont Mine. The general geology of the area is illustrated in Fig. 4.52. Data from all 8

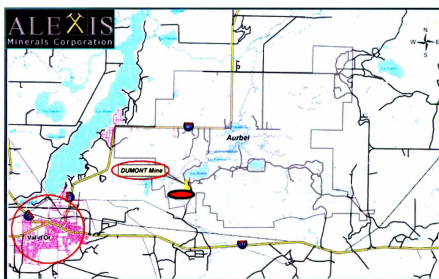


Fig. 4.51: Location of the Aurbel project (Berube, 2010).

boreholes in the area (see Fig. 4.48) were considered for inversion of DC resistivity and IP data. Based on the inversion results from single pair of boreholes, borehole data containing large amount of noise and variation were eliminated in constructing the final data set (see Fig. 4.53). Inversion of DC resistivity data showed that a half-space of the conductivity of  $0.0001 \text{ S/m}$  can be considered as the conductivity model for IP inversion. Fig. 4.54 shows that for resistivity inversion, synthetic and predicted

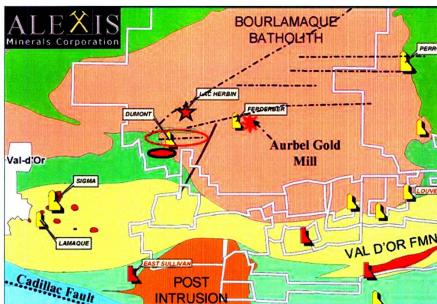


Fig. 4.52: General geology of the area (Berube, 2010).

data are suitably matched. Inversion results for hole-to-hole IP data from six pairs of boreholes, 2102-29 and 2102-30, 2102-29 and 106, 2102-29 and 125, 2102-32 and 106, 2102-33 and 125, 2102-33 and 126, (see Fig. 4.48) using Mesh B are illustrated in the Figures 4.55 after applying distance weighting. The inversion results shows three main chargeable bodies in the area. The large chargeable body located in the west is the results of previous mining activities in the area. The smaller chargeable body in the east is unknown. The small deep chargeable body in the middle was the main interest in the project (see Fig. 4.56). The inversion results were completely confirmed by Abitibi Geophysics with subsequent boreholes that were drilled in the area.

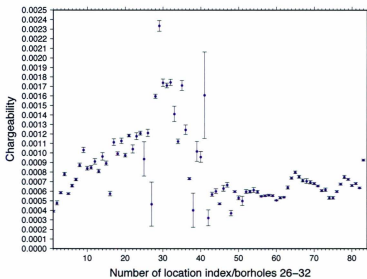


Fig. 4.53: An example of noisy data with large variation from boreholes 26-32.

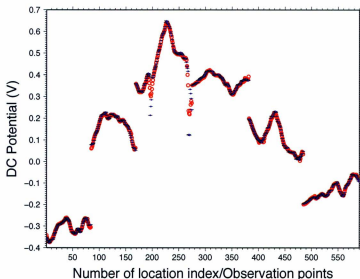


Fig. 4.54: Synthetic observed data (blue) and Predicted data (red) for the conductivity model derived from all boreholes.

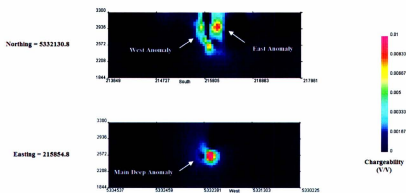


Fig. 4.55: Chargeability model constructed from the Aurbel data using distance weighting. The color scale represent the values of dimensionless chargeability.

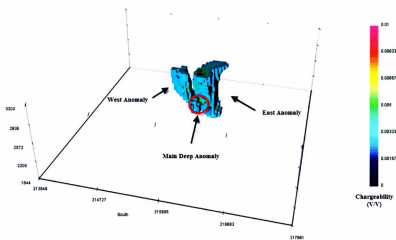
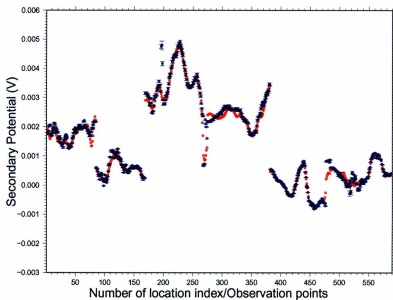
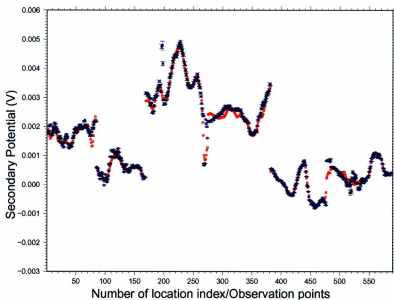


Fig. 4.56: 3D view of the chargeable targets in Aurbel property located east of Val-d'Or, Quebec, Canada.



(a) Without weighting



(b) With weighting

Figure 4.57: Observed data (blue) and predicted data (red) for the Aurbel data-set.

## Chapter 5

### 3D DC Resistivity and IP Forward Modelling based on a Surface Integral Equation

#### 5.1 Introduction

Fast and accurate 3D numerical modelling techniques are needed to fully interpret IP survey data. The late 1960s was the starting point for the development of the different numerical techniques for calculating DC resistivity and IP data such as integral equation (Dieter et al., 1969), finite element (Coggon, 1971), and finite difference methods (Mufti, 1976). The difference techniques, i.e., finite element and finite difference, are suited to modelling general Earth structures where the physical properties (e.g., electrical resistivity and chargeability) have been arbitrarily assigned different values at each mesh element in the whole grid (Snyder, 1976). Integral equation methods are most suitable for simple model geometries such as one, or at the most two, inhomogeneities of uniform conductivities imbedded in uniform half-space with a different conductivity (Snyder, 1976; Zhou and Greenhalgh, 2001; Boulanger and Chouteau, 2005). The principal benefit of the integral equation formulation compared to the difference methods is that the potential can be calculated at any point in the

3D space without any need of interpolation. Although integral equation methods are not as flexible as the difference methods in handling both complex geometry and arbitrary variations in physical properties, they are fast and accurate when a simple model is appropriate. Many researchers have been involved in the development of integral equation methods for DC and IP, and for EM data in general. For instance, Alfano (1959, 1960, 1961), Bhattacharya and Patra (1968), Pratt (1972), Raiche (1974), Hohmann (1975), Snyder (1976), Spiegel et al., (1980), Ting and Hohmann (1981), Wannamaker et al. (1984), Schulz (1985), Beasley and Ward (1986), Poirmeur and Vasseur (1988), Li and Oldenburg (1991), Xiong (1989, 1992a,b), Hvozدارa and Kaikkonen (1998). One of the most recent advancements in integral equation methods is the work of Boulanger and Chouteau (2005) in which they developed a 3D electrical resistivity modelling code for a 3D heterogeneous medium with arbitrary conductivity. They introduced a method of calculating the charge densities for an arbitrary 3D heterogeneous medium in which the volume was discretized with structured rectangular prisms of different sizes in a Cartesian system. Also, a technique was proposed to calculate the sensitivity (Jacobian) and Hessian matrices in 3D by Boulanger and Chouteau (2005). In this chapter, I present a 3D numerical modelling technique for DC resistivity and IP data that is based on a surface integral equation approach. The pivotal novelties are twofold. First, the use of unstructured meshes to describe the anomalous region. This is a more flexible approach that allows more complicated geometries to be modeled compared to a structured mesh. The non-commercial mesh

generator TetGen (Si 2003) has been employed to generate unstructured triangular meshes. Second, the 3D code has been developed for both constant and linearly varying charge density on the triangular facets of the surface of the body. The accuracy and efficiency of these two approximations will be assessed.

## 5.2 IP numerical modelling

Two general ways are widely used in IP forward modelling. The first, which is based on Seigel's theory (Seigel 1959), considers that the effect of chargeability is to change the conductivity when a current is applied. Therefore, apparent chargeability is computed by two forward DC resistivity modellings using the original and perturbed conductivity (Farias et al., 2010). The second procedure is based on the quantities originally measured in the frequency domain, including the amplitude of the apparent resistivity and the phase shift between the injected current signal and the measured voltage. In this case, a complex apparent resistivity as a complete description of these two quantities is directly modelled (Weller et al., 1996). In my code, after calculation of the accumulated charge using the integral equation formulation, the electrical potential is computed and the IP response is simulated based on the Seigel's theory which enable us to compare the results with DCIP3D code with the same approach. A brief review of Siegel's theory is covered in the next section.

### 5.2.1 Siegel's Theory

According to Siegel, the effect of applying a primary electric field in a chargeable medium is to create a volume distribution of current dipoles anti-parallel to the field at each point in the medium (Seigel, 1959). The volume current-moment strength is expressed as,

$$\mathbf{M} = -m \mathbf{J} \quad (5.1)$$

where  $\mathbf{J}$  is the primary current density and  $m$  is the constant called chargeability (see section 2.2.3.2). As illustrated in Figure 5.1, the potential from the volume dipole element of current strength  $\mathbf{M}dv$  in a medium of conductivity  $\sigma$  at a point P which is a distance  $r$  away from the dipole is

$$d\phi = \frac{1}{4\pi\sigma} \mathbf{M} \cdot \nabla \left( \frac{1}{r} \right) dv . \quad (5.2)$$

Thus, the total potential at the field point P is

$$\phi = \frac{1}{4\pi} \iiint_V \frac{\mathbf{M}}{\sigma} \cdot \nabla \left( \frac{1}{r} \right) dv , \quad (5.3)$$

where  $V$  is the volume of the chargeable region. Using Gauss's theorem and the following identity

$$\nabla \cdot \left( \frac{\mathbf{M}}{\sigma r} \right) = \frac{1}{r} \nabla \cdot \left( \frac{\mathbf{M}}{\sigma} \right) + \frac{\mathbf{M}}{\sigma} \cdot \nabla \left( \frac{1}{r} \right) , \quad (5.4)$$

the total potential can be written as

$$\phi = \frac{1}{4\pi} \iint_S \frac{\mathbf{M}_n}{\sigma r} ds - \frac{1}{4\pi} \iiint_V \frac{1}{r} \nabla \cdot \left( \frac{\mathbf{M}}{\sigma} \right) dv , \quad (5.5)$$

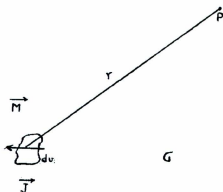


Fig. 5.1: Volume dipolar element (Seigel, 1959).

where  $S$  is the surface enclosing the volume  $V$ . Equation (5.5) shows that the effect of the volume distribution of current dipoles is equal to the sum of the effects of a volume distribution of current sources of density equal to  $-\nabla \cdot \mathbf{M}$  in regions where the conductivity of the medium is considered to be constant, and a surface distribution,  $\mathbf{M}_n$ , which is equal to the normal component of  $\mathbf{M}$  out of the surface  $S$ . The law of conservation of charge states that

$$\nabla \cdot \mathbf{J} = I\delta(\mathbf{r} - \mathbf{r}_s) \quad (5.6)$$

where  $\mathbf{J}$  is the current density vector at any point in the medium and  $I$  is the volume density of free current sources due to primary current electrodes. The effective source density  $-\nabla \cdot \mathbf{M}$  must be added to these free sources  $I$ :

$$\nabla \cdot \mathbf{J} = I - \nabla \cdot \mathbf{M} \quad \text{or} \quad \nabla \cdot (\mathbf{J} + \mathbf{M}) = I. \quad (5.7)$$

Considering the above equation and the boundary conditions, the vector  $\mathbf{J} + \mathbf{M}$ , or  $\mathbf{J}(1-m)$  from eq. (5.1), is solenoidal everywhere except in the presence of free sources

or sinks and its normal component is continuous across discontinuities in  $\sigma$  and  $m$ . From Ohm's law, the original applied current density vector is

$$\mathbf{J} = \sigma \mathbf{E} \quad (5.8)$$

where  $\mathbf{E}$  is the applied electric field caused by the external supplied sources (i.e., current electrodes). In the presence of the polarisable medium of chargeability  $m$ , the vector  $\mathbf{J}(1 - m)$  plays the role of  $\mathbf{J}$  which means that the total current density is  $\sigma(1 - m)\mathbf{E}$ . Thus, the net effect is to reduce  $\sigma$  by the factor of  $(1 - m)$ . As mentioned at the beginning of this section, the IP response can be modelled by two forward DC resistivity modellings using the original ( $\sigma$ ) and perturbed ( $\sigma(1 - m)$ ) conductivities.

### 5.3 Formulating the Surface Integral equation

The potential differences measured at the Earth's surface or down boreholes contain all the information which can be derived about the subsurface electrical structure. Having a comprehensive understanding of the whole process when the current is injected into the Earth is crucial in interpreting the results and presenting a reliable Earth's model. The two general sources of the measured potential are : (1) the potential due to the current source embedded in a homogeneous half-space; (2) the potential due to the volumetric and surface charges accumulated wherever there is a non-zero component of the electric field parallel to the gradient of conductivity. Integral equation forward modelling approaches divide the computation process into two parts. As the first step, the charge density is computed on the boundaries of

cells across which there is a conductivity contrast. Then, Coloumb's law is used to compute the potential at the observation point due to the charge accumulation (Li and Oldenburg, 1991).

### 5.3.1 Charge accumulation and Poisson's equation for the potential

DC resistivity is a steady-state problem for which

$$\nabla \times \mathbf{E} = 0, \quad \text{and} \quad (5.9)$$

$$\nabla \cdot \mathbf{D} = \rho_f, \quad (5.10)$$

where  $\mathbf{E}$  is the electric field,  $\mathbf{D}$  is the electric displacement, and  $\rho_f$  is the volumetric free charge density (Li and Oldenburg, 1991). In steady-state conditions, the divergence of the current density is equal to zero at any point except at the locations of electric current sources and sinks. So

$$\nabla \cdot \mathbf{J} = I\delta(\mathbf{r} - \mathbf{r}_s), \quad (5.11)$$

where  $I$  is the current injected, and  $r_s$  is the location of the source or sink. Also, electric displacement and current density in a linear and isotropic medium can be written in terms of electric field as

$$\mathbf{D} = \epsilon\mathbf{E}, \quad \text{and} \quad (5.12)$$

$$\mathbf{J} = \sigma\mathbf{E}, \quad (5.13)$$

where  $\sigma$  and  $\varepsilon$  are the electrical conductivity and the permittivity of the medium respectively. The boundary conditions when current flows from one medium to another with a different conductivity are

$$E_{1t} = E_{2t} , \quad \text{and} \quad (5.14)$$

$$J_{1n} = J_{2n} , \quad (5.15)$$

where  $E_{1t}$  and  $E_{2t}$  are the tangential components of the electric field, and  $J_{1n}$  and  $J_{2n}$  are the normal components of the current density on either side of the interface (see eqs. 2.11 and 2.12). In other words, the tangential component of electric field and the normal component of the current density are continuous. However, the normal components of  $\mathbf{D}$  and  $\mathbf{E}$  are not continuous because of the existence of a surface charge distribution on the boundary (Li and Oldenburg, 1991):

$$D_{2n} - D_{1n} = \tau_f , \quad \text{and} \quad (5.16)$$

$$E_{2n} - E_{1n} = \frac{\tau_t}{\varepsilon_0} \quad (5.17)$$

where the surface densities of free and total charge are represented by  $\tau_f$  and  $\tau_t$ . From eq. (5.9), the electric field in the steady-state problem can be expressed as the gradient of the scalar potential  $\phi$ :

$$\mathbf{E} = -\nabla\phi . \quad (5.18)$$

The electric field is bounded away from sources. Consequently, the potential is continuous which means the potentials in the two media at the boundary are equal,

$\phi_1 = \phi_2$  (Li and Oldenburg, 1991). Using equations (5.13) and (5.18) and substituting in (5.11) we have

$$\nabla \cdot (\sigma \nabla \phi) = -I \delta(\mathbf{r} - \mathbf{r}_s) \quad (5.19)$$

which can be expanded and rearranged to

$$\nabla^2 \phi = -\frac{\nabla \sigma \cdot \nabla \phi}{\sigma} - \frac{I}{\sigma} \delta(\mathbf{r} - \mathbf{r}_s). \quad (5.20)$$

Equation (5.20) is Poisson's equation. Both terms on the right-hand side of the equation can be considered as charge densities since they have the units of  $\rho/\epsilon_0$  (Li and Oldenburg, 1991). The first term corresponds to the charge build up that results whenever there is a component of the electrical field parallel to the conductivity gradient. The volumetric density of the charge accumulation under these circumstances is

$$\rho_t = \epsilon_0 \frac{\nabla \sigma \cdot \nabla \phi}{\sigma}. \quad (5.21)$$

At the interface between two media where there is a discontinuity in conductivity, the volumetric charge density transforms into a surface charge density confined to the boundary surface. Therefore, normal components of  $\mathbf{D}$  and  $\mathbf{E}$  are discontinuous in this situation. Using Ohm's law (eq. 5.8) with the combination of equations (5.15) and (5.17), the total surface charge density can be written as

$$\frac{\tau_t}{\epsilon_0} = \left(1 - \frac{\sigma_2}{\sigma_1}\right) E_{2n}. \quad (5.22)$$

The sign of the accumulated charge can be predicted using the above equation. For instance, negative charges build up when the current flows from a resistive into a

conductive region. Based on equation (5.20), the governing parameter in charge accumulation is conductivity while permittivity does not play any role. When an electric field is applied to a polarisable medium, an electric polarization is generated which is given by

$$\mathbf{P} = \chi \varepsilon_0 \mathbf{E} . \quad (5.23)$$

$\mathbf{P}$  is the polarization vector and  $\chi = (\varepsilon/\varepsilon_0) - 1$  is the electric susceptibility. Under these condition, the polarization charge at the boundary of the medium is

$$\tau_b = \mathbf{P} \cdot \mathbf{n} , \quad (5.24)$$

where  $\mathbf{n}$  is the outward unit normal vector. The net polarization charge at the interface of two regions with different permittivities is

$$\tau_b = -(P_{2n} - P_{1n}) . \quad (5.25)$$

The total accumulated charge is the polarization charge plus the free charge. Substituting (5.12) into (5.16) and (5.23) into (5.25) and doing summation yields

$$\tau_t = \varepsilon_0 (E_{2n} - E_{1n}) , \quad (5.26)$$

which is exactly the same as eq. (5.17). Consequently, in the case of a polarisable medium, both free and polarization charges contribute to the total accumulation charge. Although the total accumulated charge is controlled only by electrical conductivity, the permittivity determines how much free charge has to be accumulated to satisfy the boundary conditions (Li and Oldenburg, 1991).

### 5.3.2 A Surface Integral Equation for the charge density

For any continuous functions  $\phi$  and  $G$  with derivatives up to second order, Green's second identity states that (Li and Oldenburg, 1991)

$$\iiint_V (\phi \nabla^2 G - G \nabla^2 \phi) dv = \oint_S \left( \phi \frac{\partial G}{\partial n} - G \frac{\partial \phi}{\partial n} \right) ds. \quad (5.27)$$

In our case,  $\phi$  is chosen to be a potential function which satisfies eq. (5.20) and  $G$  to be the Green's function for a homogeneous half-space:

$$G(\mathbf{r} - \mathbf{r}') = \frac{1}{|\mathbf{r} - \mathbf{r}'|} + \frac{1}{|\mathbf{r} - \mathbf{r}''|}, \quad (5.28)$$

where  $\mathbf{r}''$  is the reflection of the point  $\mathbf{r}'$  across the half-space boundary (Snyder, 1976). Within the bounds of the volume of the anomalous region,  $V$ , both  $\phi$  and  $G$  are functions of inverse distance from the source and their normal derivatives on the boundary of  $V$  (i.e.,  $\frac{\partial G}{\partial n}$  and  $\frac{\partial \phi}{\partial n}$ ) are functions of inverse distance squared. Therefore, as  $S$ , which is the closed surface that surrounds volume  $V$ , approaches infinity, the right-hand side of the equation (5.27) vanishes. Substituting eq. (5.20) into (5.27) gives

$$\phi(\mathbf{r}) = \frac{I}{4\pi\sigma_s} G(\mathbf{r}, \mathbf{r}_s) + \iiint_V \frac{\nabla\sigma(\mathbf{r}') \cdot \nabla\phi(\mathbf{r}')}{\sigma} G(\mathbf{r}, \mathbf{r}') dv, \quad (5.29)$$

where  $\sigma_s$  is the conductivity of the half-space. The first term on the right-hand side of eq. (5.29) is the potential due to the point source in a uniform half-space of conductivity  $\sigma_s$ . The potential due to the accumulated charge distribution is given by the second term. To make a numerical solution possible, the conductivity structure is considered to be piecewise constant. Thus, except at boundaries between regions

with different conductivities,  $\nabla\sigma$  is zero. As a result, the volume integral in eq. (5.29) transforms to a set of surface integrals containing the surface charge densities (Li and Oldenburg, 1991):

$$\phi(\mathbf{r}) = \frac{I}{4\pi\sigma_s}G(\mathbf{r}, \mathbf{r}_s) + \frac{1}{4\pi} \sum_{i=1}^N \iint_{\Gamma_i} \frac{\tau_i(\mathbf{r}')}{\varepsilon_0} G(\mathbf{r}, \mathbf{r}') ds, \quad (5.30)$$

where  $\tau_i$  is the charge density on the  $i$ th boundary of the closed surface  $\Gamma_i$  and  $N$  is the number of regions on the anomalous body surface with different charge densities.

The normal component of the electric field in the background is :

$$E_n = -\mathbf{n}_j \cdot \nabla\phi, \quad (5.31)$$

where  $\mathbf{n}_j$  is the unit outward normal of the  $j$ th boundary. Combining the above equation with eq. (5.22), charge density on the  $j$ th boundary can be written as

$$\frac{\tau_j}{\varepsilon_0} = \frac{\sigma_s - \sigma_j}{\sigma_j} \mathbf{n}_j \cdot \nabla\phi. \quad (5.32)$$

Since equation (5.32) is valid everywhere, the integral equation for the charge accumulation can be simply obtained by substituting eq. (5.30) into eq. (5.32) to eliminate the potential:

$$\frac{\sigma_j}{\sigma_s - \sigma_j} \cdot \frac{\tau_j(\mathbf{r})}{\varepsilon_0} = \frac{I}{4\pi\sigma_s} \mathbf{n}_j \cdot \nabla G(\mathbf{r}, \mathbf{r}_s) + \frac{1}{4\pi} \sum_{i=1}^N \iint_{\Gamma_i} \frac{\tau_i(\mathbf{r}')}{\varepsilon_0} \mathbf{n}_j \cdot \nabla G(\mathbf{r}, \mathbf{r}') ds, \quad (5.33)$$

where  $\mathbf{r} \in \Gamma_j$ ,  $\mathbf{n}_j = \mathbf{n}_j(\mathbf{r})$  and  $j = 1, 2, 3, \dots, N$ . Notice that the gradient operates on the field point  $\mathbf{r}$  while the integrals operate on the secondary source points  $\mathbf{r}'$  (Li and Oldenburg, 1991).

### 5.3.3 Singularity removal

The surface integral in eq. (5.33) is improper because the integrand is infinite when  $\mathbf{r} \rightarrow \mathbf{r}'$ . The singularity occurs only for  $i = j$ , i.e.,  $\Gamma_i = \Gamma_j$ . This singularity is straightforward to remove. By expanding the improper integral into its components, we have (Snyder, 1976)

$$\begin{aligned} \frac{\sigma_j}{\sigma_s - \sigma_j} \cdot \frac{\tau_j}{\epsilon_0} &= \frac{I}{4\pi\sigma_s} \mathbf{n}_j \cdot \nabla G(\mathbf{r}, \mathbf{r}_s) \\ &+ \frac{1}{4\pi} \iint_{\Gamma_j} \frac{\tau_j(\mathbf{r}')}{\epsilon_0} \mathbf{n}_j \cdot \nabla \frac{1}{|\mathbf{r} - \mathbf{r}'|} ds \\ &+ \frac{1}{4\pi} \iint_{\Gamma_j} \frac{\tau_j(\mathbf{r}')}{\epsilon_0} \mathbf{n}_j \cdot \nabla \frac{1}{|\mathbf{r} - \mathbf{r}''|} ds \\ &+ \frac{1}{4\pi} \sum_{i \neq j} \iint_{\Gamma_i} \frac{\tau_i(\mathbf{r}')}{\epsilon_0} \mathbf{n}_j \cdot \nabla G(\mathbf{r}, \mathbf{r}') ds \end{aligned} \quad (5.34)$$

which shows that only the first integral is singular. One approach to remove the singularity is to divide the surface of the first integral into  $\Gamma'_j$  which excludes the singularity ( $\mathbf{r} = \mathbf{r}'$ ) plus an arbitrary small disk  $\Gamma_\delta$  of radius  $\delta$  centered about ( $\mathbf{r} = \mathbf{r}'$ ):

$$\begin{aligned} \frac{1}{4\pi} \iint_{\Gamma_j} \frac{\tau_j(\mathbf{r}')}{\epsilon_0} \mathbf{n}_j \cdot \nabla \frac{1}{|\mathbf{r} - \mathbf{r}'|} ds &= \\ &\frac{1}{4\pi} \iint_{\Gamma_\delta} \frac{\tau_j(\mathbf{r}')}{\epsilon_0} \mathbf{n}_j \cdot \nabla \frac{1}{|\mathbf{r} - \mathbf{r}'|} ds \\ &+ \frac{1}{4\pi} \iint_{\Gamma'_j} \frac{\tau_j(\mathbf{r}')}{\epsilon_0} \mathbf{n}_j \cdot \nabla \frac{1}{|\mathbf{r} - \mathbf{r}'|} ds. \end{aligned} \quad (5.35)$$

Since the singular point has been excluded from the integration domain, the second integral on the right-hand side of eq. (5.35) is proper. The electric charge over the area in the first integral can be essentially regarded as a constant value ( $\tau_j(\mathbf{r} = \mathbf{r}') \simeq \tau_j$ ) since the area of  $\Gamma_\delta$  can be considered sufficiently small. Thus,

$$\frac{1}{4\pi} \iint_{\Gamma_\delta} \frac{\tau_j(\mathbf{r}')}{\epsilon_0} \mathbf{n}_j \cdot \nabla \frac{1}{|\mathbf{r} - \mathbf{r}'|} ds \simeq \frac{\tau_j}{4\pi\epsilon_0} \iint_{\Gamma_\delta} \mathbf{n}_j \cdot \nabla \frac{1}{|\mathbf{r} - \mathbf{r}'|} ds. \quad (5.36)$$

Performing the integral is more convenient in a cylindrical coordinate system whose origin is located at the centre of the disk  $\Gamma_\delta$  and whose  $z$  axis coincides with the unit normal  $\mathbf{n}_j$ . Also, it is beneficial to allow the point  $r$  to be located on the  $z$  axis a small distance ( $z$ ) above the disk which is allowed to approach zero after performing the integral (Snyder 1976). By interchanging the order of integration and differentiation, the integral can be written as

$$\begin{aligned} \tau_j(\mathbf{r}) \int_0^\delta \int_0^{2\pi} \mathbf{n}_j \cdot \nabla \frac{1}{|\mathbf{r}-\mathbf{r}'|} ds &= \tau_j(\mathbf{r}) \ 2\pi \ \frac{\partial}{\partial z} \int_0^\delta \frac{r}{[r^2+z^2]^{1/2}} dr \quad (5.37) \\ &= \tau_j(\mathbf{r}) \ 2\pi \ \lim_{z \rightarrow 0} \frac{\partial}{\partial z} \{[\delta^2+z^2]^{1/2} - z\} \\ &= \tau_j(\mathbf{r}) \ 2\pi \ \lim_{z \rightarrow 0} \left\{ \frac{z}{[\delta^2+z^2]^{1/2}} - 1 \right\} = -2\pi \ \tau_j(\mathbf{r}) . \end{aligned}$$

After applying the singularity removal, equation (5.33) can be written as

$$\begin{aligned} \frac{\tau_j(\mathbf{r})}{\varepsilon_0} &= \frac{Ik_j}{2\pi\sigma_s} \mathbf{n}_j \cdot \nabla G(\mathbf{r}, \mathbf{r}_s) + \frac{k_j}{2\pi} \sum_{i \neq j}^N \iint_{\Gamma_i} \frac{\tau_i(\mathbf{r}')}{\varepsilon_0} \mathbf{n}_j \cdot \nabla G(\mathbf{r}, \mathbf{r}') ds \quad (5.38) \\ &\quad + \frac{k_j}{2\pi} \iint_{\Gamma_j'} \frac{\tau_j(\mathbf{r}')}{\varepsilon_0} \mathbf{n}_j \cdot \nabla G(\mathbf{r}, \mathbf{r}') ds , \end{aligned}$$

where  $k_j = (\sigma_s - \sigma_j)/(\sigma_s + \sigma_j)$  and  $\Gamma_j'$  is the  $j$ th boundary with a small area around point  $r$  excluded. All integrals in eq. (5.38) are now proper (Li and Oldenburg, 1991).

#### 5.4 3D Surface integral equation forward modelling code

The geometry of the problem is illustrated in Fig. 5.2. The Earth model is the homogeneous half-space of conductivity  $\sigma_1$  and chargeability  $m_1$  in which a 3D body of conductivity  $\sigma_2$  and chargeability  $m_2$  is embedded. The approach is to triangularize the surface of the body using the unstructured mesh generator TetGen (Si, 2003),

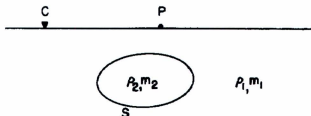


Fig. 5.2: Geometry of the Earth model for the surface integral forward modelling where C and P are the current and potential electrodes respectively and S is the surface of the anomaly (Dieter et al., 1969).

calculate the accumulated electrical charge density (eq. 5.38) over each triangular element numerically, and calculate the electrical potential at any point either at the Earth's surface or in the halfspace by substituting the charge density into eq. (5.30). Having the electrical potential, both DC resistivity data and IP responses can be modelled. As illustrated in Fig. 5.2, the pole-pole configuration is used to calculate the synthetic data in the subsequent examples.

#### 5.4.1 Numerical calculation of a surface integral over an arbitrary 3D triangle

Computing the surface integral in eq. (5.38) over a triangular facet with an arbitrary orientation in 3D space is a cumbersome procedure. Since the electrical potential is not affected by parallel translation or rotation of the coordinate system (Okabe, 1979), one way to overcome this difficulty is to transform the arbitrarily oriented 3D triangle to the 2D standard triangle in the  $X - Y$  plane with normal in  $Z$  direction i.e., with vertices of  $(0, 0)$ ,  $(1, 0)$ , and  $(0, 1)$ . As the first action, the surface Cartesian system

$(X, Y, Z)$  must be defined where the  $Z$ -direction is coincident with the direction of the outward unit normal vector of the triangular element  $\Gamma_i$ . This is a two step procedure (see Fig. 5.3). First, the  $x$ - and  $y$ - axes must be rotated through the

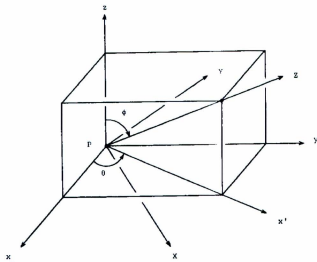


Fig. 5.3: The surface rotation of the Cartesian system (Okabe 1979)

angle  $\theta$  around the  $z$ -axis until the rotated  $x$ -axis points in the same direction as the projected direction of the outward normal on to the  $x$ - $y$  plane. Obviously,  $\theta$  is equal to zero if the  $z$ -axis is already perpendicular to the facet. Second, the  $z$ - and  $x$ -axes must be rotated through the angle  $\phi$  around the  $Y$ -axis until the rotated  $z$ -direction is coincident with the direction of the outward normal. Notice that all rotations are counterclockwise. At this point, the desired system  $(X, Y, Z)$  is obtained (Okabe,

1979). The coordinate transformation can be written as

$$\begin{bmatrix} X \\ Y \\ Z \end{bmatrix} = \begin{bmatrix} \cos \phi & 0 & -\sin \phi \\ 0 & 1 & 0 \\ \sin \phi & 0 & \cos \phi \end{bmatrix} \begin{bmatrix} \cos \theta & \sin \theta & 0 \\ -\sin \theta & \cos \theta & 0 \\ 0 & 0 & 1 \end{bmatrix} = \begin{bmatrix} x \\ y \\ z \end{bmatrix} \quad (5.39)$$

where  $0 \leq \theta \leq 2\pi$  and  $0 \leq \phi \leq \pi$ .  $Z$  is constant over the transformed surface which allows us to consider it as a 2D triangle in the  $(X, Y)$  coordinate system. Using the projection of a triangular surface illustrated in Fig. 5.4, angles  $\theta$  and  $\phi$  can be defined as (Okabe, 1979)

$$\cos \theta = -S_{yz}/(S_{yz}^2 + S_{zx}^2)^{1/2} \quad (5.40)$$

$$\sin \theta = -S_{zx}/(S_{yz}^2 + S_{zx}^2)^{1/2}$$

and

$$\cos \phi = -S_{xy}/(S_{yz}^2 + S_{zx}^2 + S_{xy}^2)^{1/2} \quad (5.41)$$

$$\sin \phi = [(S_{yz}^2 + S_{zx}^2)/(S_{yz}^2 + S_{zx}^2 + S_{xy}^2)]^{1/2}$$

where  $S_{yz}$ ,  $S_{zx}$ , and  $S_{xy}$  are twice the projected areas of the triangular surface onto the  $yz$ ,  $zx$ , and  $xy$  planes respectively (see Fig. 5.4). For instance

$$S_{xy} = x_1(y_2 - y_3) + x_2(y_3 - y_1) + x_3(y_1 - y_2). \quad (5.42)$$

It should be noted that both primary and transformed triangles must be right-handed. Hence, twice the area defined by

$$T = X_1(Y_2 - Y_3) + X_2(Y_3 - Y_1) + X_3(Y_1 - Y_2) \quad (5.43)$$

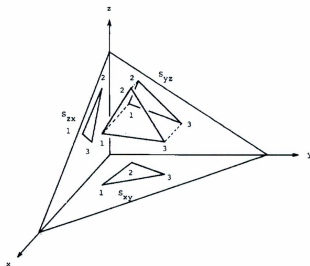


Fig. 5.4: The projection of a triangular surface (Okabe 1979)

must be negative. While applying the coordinate transformation in the integration process, the absolute value of the Jacobian should be multiplied to the integrand.

The Jacobian can be formulated as

$$J = \det \left\{ \frac{\partial(x, y, z)}{\partial(X, Y, Z)} \right\}, \quad (5.44)$$

which is equal to 1 for the first coordinate transformation given by eq. (5.39). The next transformation which must be carried out to obtain the standard triangle is

$$\begin{aligned} x' &= \frac{\Delta}{2\beta}(a_1 + b_1X + c_1Y), \\ y' &= \frac{\Delta}{2\beta}(a_2 + b_2X + c_2Y), \end{aligned} \quad (5.45)$$

where

$$\begin{aligned}
 a_1 &= X_2 Y_3 - Y_2 X_3 & b_1 &= Y_2 - Y_3 & c_1 &= X_3 - X_2 \\
 a_2 &= X_3 Y_1 - Y_3 X_1 & b_2 &= Y_3 - Y_1 & c_2 &= X_1 - X_3 \\
 a_3 &= X_1 Y_2 - Y_1 X_2 & b_3 &= Y_1 - Y_2 & c_3 &= X_2 - X_1
 \end{aligned} \tag{5.46}$$

$\Delta$  is the area of the triangle element, which is defined by

$$\Delta = \frac{1}{2} \begin{vmatrix} 1 & X_1 & Y_1 \\ 1 & X_2 & Y_2 \\ 1 & X_3 & Y_3 \end{vmatrix} = \frac{1}{2}(b_1 c_2 - b_2 c_1), \tag{5.47}$$

and  $\beta$  is

$$\beta = \frac{\Delta}{2}(b_1 X_1 + b_2 X_2 + b_3 X_3). \tag{5.48}$$

Based on eq. (5.44), the Jacobian for this transformation is given by

$$J = \frac{2\beta^2}{\Delta^3}. \tag{5.49}$$

A Gauss-Legendre quadrature method is used for numerical evaluation of the resulting integral (Rathod et al., 2007). The integral over the standard triangle, i.e.,

$$I = \iint_T f(x', y') dx' dy' = \int_0^1 dx' \int_0^{1-x'} f(x', y') dy' \tag{5.50}$$

is transformed into an integral over the standard 1-square by the change of variables (see Fig. 5.5):

$$x' = uv, \quad , \quad y' = u(1-v). \tag{5.51}$$

The differential area and Jacobian determinant for the new integral are

$$J = \frac{\partial(x', y')}{\partial(u, v)} = -u, \quad (5.52)$$

$$dx' dy' = -u du dv,$$

This integral can be further transformed into an integral over the standard 2-square (see Fig. 5.5) by the change of variables:

$$u = \frac{(1 + \zeta)}{2}, \quad v = \frac{(1 + \eta)}{2} \quad (5.53)$$

for which the Jacobian and differential area are

$$J = \frac{\partial(u, v)}{\partial(\zeta, \eta)} = 1/4, \quad (5.54)$$

$$du dv = 1/4 d\zeta d\eta.$$

Thus, the integral over the standard triangle (see eq. 5.50) can be written as:

$$I = \int_{-1}^1 \int_{-1}^1 f\left(\frac{(1 + \zeta)(1 + \eta)}{4}, \frac{(1 + \zeta)(1 - \eta)}{4}\right) \left(\frac{1 + \zeta}{8}\right) d\zeta d\eta. \quad (5.55)$$

For the integral over the 2-square, efficient Gauss-Legendre quadrature methods are available for any desired accuracy (see Appendix A). The integral  $I$  can be numerically computed as

$$I = \sum_{i=1}^s \sum_{j=1}^s \left(\frac{1 + \zeta_i}{8}\right) w_i w_j f(x'(\zeta_i, \eta_j), y'(\zeta_i, \eta_j)) \quad (5.56)$$

where  $\zeta_i, \eta_j$  are Gaussian points and  $w_i$  and  $w_j$  are the corresponding weight coefficients. Equation (5.56) can be rewritten as

$$I = \sum_{k=1}^N = s \times sc_k f(x_k, y_k) \quad (5.57)$$

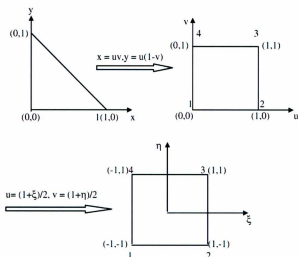


Fig. 5.5: Transformation of standard triangle  $T$  into equivalent unit square in  $(u, v)$  space and 2-square in  $(\zeta, \eta)$  space (Rathod et al., 2007).

where  $c_k, x_k$ , and  $y_k$  can be obtained from the relations

$$c_k = \left( \frac{1 + \zeta_i}{8} \right) w_i w_j, \quad (5.58)$$

$$x_k = \frac{(1 + \zeta_i)(1 + \eta_j)}{4}, \quad y_k = \frac{(1 + \zeta_i)(1 - \eta_j)}{4} \quad (5.59)$$

where  $k = 1, 2, 3, \dots, N$  and  $i, j = 1, 2, 3, \dots, n$  (Rathod et al., 2007).

#### 5.4.2 3D forward modelling code for piecewise constant electric charge

In order to develop a numerical solution for charge density and hence potential, the charge density must be discretized. One choice is to assume that the charge density is constant over each triangular facet. Substitution of this representation for the charge density into the integral equation eq. (5.38) yields a system of linear equations to be

solved for the charge densities on the facets (Li and Oldenburg, 1991). Considering  $M$  as the number of elements and a constant charge  $\tau_i$  assigned to the  $i$ th element, eq. (5.38) yields

$$\frac{\tau_j}{\varepsilon_0} = \frac{Ik_j}{2\pi\sigma_s} \frac{\partial G(\mathbf{r}_j, \mathbf{r}_s)}{\partial n_j} + \frac{k_j}{2\pi} \sum_{i \neq j}^M \frac{\tau_i}{\varepsilon_0} \iint_{\Gamma_i} \frac{\partial G(\mathbf{r}_j, \mathbf{r}')}{\partial n_j} ds + \frac{k_j \tau_j}{2\pi\varepsilon_0} \iint_{\Gamma_j} \frac{\partial G(\mathbf{r}_j, \mathbf{r}')}{\partial n_j} ds \quad (5.60)$$

$j = 1, 2, 3, \dots, M,$

where  $\mathbf{r}_j$  denotes the centre of gravity of the  $j$ th element,  $\tau_j = \tau(\mathbf{r}_j)$  is the charge density at  $\mathbf{r}_j$ , and  $\mathbf{n}_j$  is the outward unit normal vector of this element. Equation (5.60) can be written in matrix form as

$$\mathbf{A}\boldsymbol{\tau} = \mathbf{B}, \quad (5.61)$$

where  $\mathbf{A}$  is an  $M \times M$  coefficient matrix with components

$$A_{jj} = \frac{1}{\varepsilon_0} - \frac{k_j}{2\pi\varepsilon_0} \iint_{\Gamma_j} \frac{\partial G(\mathbf{r}_j, \mathbf{r}')}{\partial n_j} ds, \quad (5.62)$$

and

$$A_{ji} = \frac{k_j}{2\pi\varepsilon_0} \iint_{\Gamma_i} \frac{\partial G(\mathbf{r}_j, \mathbf{r}')}{\partial n_j} ds, \quad (5.63)$$

$\boldsymbol{\tau}$  is the  $M \times 1$  vector of unknown charge densities, and  $\mathbf{B}$  is the  $M \times 1$  vector with components

$$B_j = \frac{Ik_j}{2\pi\sigma_s} \frac{\partial G(\mathbf{r}_j, \mathbf{r}_s)}{\partial n_j}. \quad (5.64)$$

After calculations of the components of matrices  $\mathbf{A}$  and  $\mathbf{B}$ , the matrix equation (5.61) is solved using the freely available direct solver (dgesv.f) from the online mathematical library LAPACK (Dongarra et. al., 2002) (see Appendix B).

### 5.4.3 3D forward modelling code for linearly varying electric charge

Another approach to approximate the unknown charge density is to assume that the electric charge is linearly varying within each triangular facet. For 3D linear triangular elements, the unknown function  $\tau$  within each element is approximated as (Jin, 2002):

$$\tau^e(x, y, z) = \sum_{j=1}^3 N_j^e(x, y, z) \tau_j^e \quad j = 1, 2, 3 \quad (5.65)$$

where  $e$  is the facet number and  $j$  is the vertex number for triangular facet.  $N_j^e(x, y, z)$  are the interpolation functions given by

$$N_j^e(x, y, z) = \frac{1}{2\Delta^e} (a_j^e + N_x^e x_j^e + N_y^e y_j^e + N_z^e z_j^e) \quad (5.66)$$

where  $x_j^e, y_j^e$  and  $z_j^e$  denote the coordinates of the  $j$ th vertex of the  $e$ th facet and  $\Delta^e$  is its area. Also,

$$N_x^e = b_j \cos \theta \cos \phi - c_j \sin \theta \quad (5.67)$$

$$N_y^e = b_j \sin \theta \cos \phi + c_j \cos \theta$$

$$N_z^e = -b_j \sin \phi$$

where  $b_j, c_j, \theta$ , and  $\phi$  were previously introduced in Section 5.4.1. The interpolation functions have the property

$$N_i^e(x_j^e, y_j^e, z_j^e) = \delta_{ij} = \begin{cases} 1 & i = j \\ 0 & i \neq j \end{cases} \quad (5.68)$$

Consequently,  $\tau^e$  in eq. (5.65) reduces to its nodal value  $\tau_i^e$  at node  $i$ . Moreover,  $N_j^e(x, y, z)$  vanishes for a point located on the facet edge opposite the  $j$ th node. Therefore, the value of  $\tau$  on each facet edge is determined by its value at the two endpoints and is not related to its value at the opposite node. This important feature guaranties continuity of the charge density across the facet edges (Jin, 2002). To obtain the proper system of linear equations, a global numbering approach must be considered for the facets and their vertices, i.e., nodes. Thus, the value of  $\tau_j$  is assigned to each node; however, each node shares different interpolation functions from each neighboring facet that shares that node. The value of the surface integral in eq. (5.38) for each node is the summation of the integral over all the facets sharing that node. By these definitions, and substituting the linear representation of the charge density into eq. (5.38), the final system of equations is obtained as

$$\begin{aligned} \frac{\tau_j}{\varepsilon_0} = & \frac{Ik_j}{2\pi\sigma_s} \mathbf{n}_j \cdot \nabla G(\mathbf{r}_j, \mathbf{r}_s) + \frac{k_j \tau_i}{2\pi\varepsilon_0} \sum_{i \neq j}^N \sum_{e=1}^E \iint_{\Gamma_i} N_i^e(\mathbf{r}') \mathbf{n}_j \cdot \nabla G(\mathbf{r}_j, \mathbf{r}') ds \\ & + \frac{k_j \tau_j}{2\pi\varepsilon_0} \sum_{e=1}^E \iint_{\Gamma_j^e} N_j^e(\mathbf{r}') \mathbf{n}_j \cdot \nabla G(\mathbf{r}_j, \mathbf{r}') ds, \\ & j = 1, 2, 3, \dots, N, \end{aligned} \quad (5.69)$$

where  $\mathbf{r}_j$  denotes the location of the  $j$ th node, and  $N_j^e(\mathbf{r}')$  is the interpolation function associated with node  $j$  in the facet  $e$ . The number of nodes is  $N$ , and  $E$  is the number of neighboring facets for a node, which obviously has different values for different nodes. Rearranging eq. (5.69) yields the matrix equation

$$\mathbf{A}\boldsymbol{\tau} = \mathbf{B} \quad (5.70)$$

where  $\mathbf{A}$  is an  $N \times N$  coefficient matrix with components

$$A_{jj} = \frac{1}{\epsilon_0} - \frac{k_j}{2\pi\epsilon_0} \sum_{e=1}^E \iint_{\Gamma'_j} N_j^e(\mathbf{r}') \mathbf{n}_j \cdot \nabla G(\mathbf{r}_j, \mathbf{r}') ds \quad (5.71)$$

and

$$A_{ji} = \frac{k_j}{2\pi\epsilon_0} \sum_{e=1}^E \iint_{\Gamma_i} N_i^e(\mathbf{r}') \mathbf{n}_j \cdot \nabla G(\mathbf{r}_j, \mathbf{r}') ds, \quad (5.72)$$

$\tau$  is the  $N \times 1$  vector of unknown values of the charge densities at the nodes, and  $\mathbf{B}$  is the  $N \times 1$  vector with components

$$B_j = \frac{Ik_j}{2\pi\sigma_s} \mathbf{n}_j \cdot \nabla G(\mathbf{r}_j, \mathbf{r}_s). \quad (5.73)$$

It should be noted that in this node based approach,  $\mathbf{n}_j$  denotes the outward unit normal vector at the  $j$ th node. Two different techniques are implemented to derive the nodal outward normal vector. The first averages outward unit normal vectors of all neighboring facets. The other approach is to fit a sphere to that node and its neighboring nodes to derive the nodal outward normal vector using the direction of the radius of the sphere at the location of the node. Each technique has its own advantages based on the shape of the 3D anomaly as will be shown bellow. Again, the matrix equation is solved using the freely available direct solver (dgesv.f) from the online mathematical library LAPACK (Dongarra et. al., 2002)(see Appendix B).

## 5.5 Example 1: Potential due to a buried conductive sphere

### 5.5.1 Analytical formula for the potential due to a sphere in a uniform field

One of the few three-dimensional bodies for which the exact solution has been developed in electrical resistivity theory is the sphere. The problem is finding the potential distribution on the surface of a uniform half-space in which a conductive sphere is embedded (see Fig. 5.6). It is easier to work in spherical coordinates with the sphere

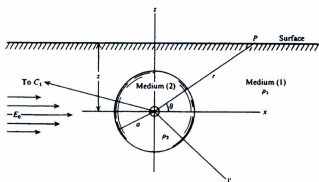


Fig. 5.6: Buried conducting sphere in uniform field.  $a$  is the radius of the sphere,  $\rho_2$  is the resistivity of the sphere and  $\rho_1$  is the resistivity of the halfspace (Telford et al., 1990).

centre as origin and the polar axis parallel to the  $x$ -axis. In order to derive an analytic solution, the sphere is assumed to be in a uniform electric field  $E_0$  parallel to the  $x$ -axis which is equivalent to having the current electrodes far to the left or right of the sphere in Fig. 5.6. By solving Laplace's equation in spherical coordinates and applying the boundary conditions, the potential at the surface is obtained (Telford

et al., 1990). For  $r > a$

$$\phi = -E_0 r \cos \theta \left\{ 1 - \frac{(\rho_1 - \rho_2)}{(\rho_1 + 2\rho_2)} \left( \frac{a}{r} \right)^3 \right\}. \quad (5.74)$$

The second term in eq. (5.74) will be doubled if the potential is measured at the ground surface because of the sphere image reflected by the half-space boundary.

Considering the field generated by a current source  $C_1$  at a distance  $R$  from the centre of the sphere, eq. (5.74) can be rewritten as

$$\phi = -\frac{I\rho_1}{2\pi R^2} \left\{ 1 - 2\frac{(\rho_1 - \rho_2)}{(\rho_1 + 2\rho_2)} \left( \frac{a}{r} \right)^3 \right\} r \cos \theta \quad (5.75)$$

which denotes the total potential measured at the surface. Notice that the disturbing potential due to the conductive sphere is shown by the second term (Telford et al. 1990). Two important conditions must be considered while comparing the results from the analytic expression above and the 3D forward modelling code developed in the preceding sections. Firstly, the external or background field is considered to be uniform, which can be approximated by increasing the distance between the sphere and the current source. Secondly, no interaction between the sphere and its image has been taken into account. For this to be valid, the distance between the sphere's centre and the surface should not be less than 1.3 times its radius.

### 5.5.2 3D Numerical solution for the potential due to a sphere in a uniform field

The discretized sphere for which the problem has been solved is illustrated in Fig. 5.7. The geometry of the problem is the same as illustrated in Fig. 5.2. The pole-

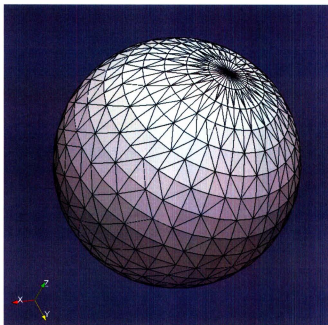


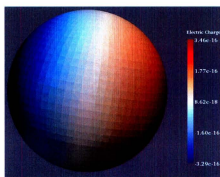
Fig. 5.7: Discretized sphere for the example presented in Section 5.5 with 1520 triangular facets and 762 nodes.

pole configuration is used, and the current electrode injects a current of 1A into the ground. The conductivity of the half-space is  $10^{-4}$  S/m and the conductivity of the sphere is 1 S/m. Neither the half-space nor the sphere are polarisable (i.e.,  $m_1$  and  $m_2 = 0$ ). The coordinate values of the centre of the sphere are (1225, 350, -550) m

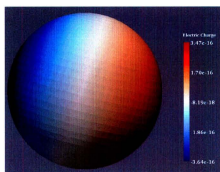
and the radius of the sphere is 195 m. The measuring profile is parallel to the  $x$ -axis directly over the center of the sphere, that is the  $y$ - and  $z$ - coordinates of the potential electrodes are 350 m and 0.0 m respectively. The distance between two successive potential electrodes is 10 m and the potential was calculated at 251 locations. The starting location of the profile is (0, 350, 0) m and the ending point is (-2500, 350, 0) m.

#### 5.5.2.1 Charge Accumulation over the 3D spherical anomaly

Based on eq. (5.22), negative charges build up when the current flows from a resistive into conductive region. As the buried sphere is more conductive than the surrounding medium, the negative charge must be accumulated as the current flows from the half-space through the sphere and the positive charge must be accumulated as the current is passing from the sphere to the half-space. The exact behavior can be produced by the developed 3D code which is illustrated in Fig. 5.8 for both constant and linearly varying distribution of electric charge where conductivity of the half-space is  $10^{-4}$  S/m and the conductivity of the sphere is 1 S/m. For this example the sphere is discretized into 4106 facets and 2055 nodes.



(a) Constant Charge



(b) Linearly varying charge

Figure 5.8: Charge accumulation, in coulomb (C), over a conductive sphere in a resistive background.

### 5.5.2.2 Different location of current source

The calculated potential due to the conductive buried sphere is presented for different locations of the current source. By increasing the distance between the centre of the sphere and the current electrode, the condition of having uniform electric field at the location of the sphere is better approximated. In this example, the number of the facets is 1520 and the number of nodes is 762. Results were calculated for both constant and linearly varying charge distributions for four different locations of the current sources :  $(-50, 350, 0)$  m,  $(-1000, 350, 0)$  m ,  $(-5000, 350, 0)$  m, and  $(-10000, 350, 0)$  m. The observation locations are along the  $x$ -axis on the surface of the halfspace (see Figs. 5.9 to 5.12).

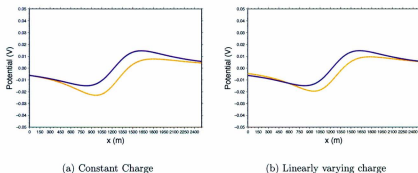


Figure 5.9: DC resistivity potential due to conductive buried sphere using pole-pole configuration for a source location of  $(-50, 350, 0)$  m: analytic response (blue), 3D forward modelling code (orange).

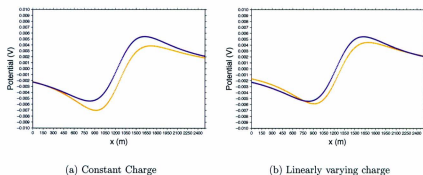


Figure 5.10: DC resistivity potential due to conductive buried sphere using pole-pole configuration for a source location of  $(-1000, 350, 0)$  m: analytic response (blue), 3D forward modelling code (orange).

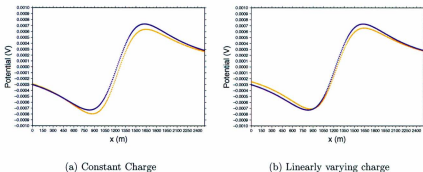


Figure 5.11: DC resistivity potential due to conductive buried sphere using pole-pole configuration for a source location of  $(-5000, 350, 0)$  m: analytic response (blue), 3D forward modelling code (orange).

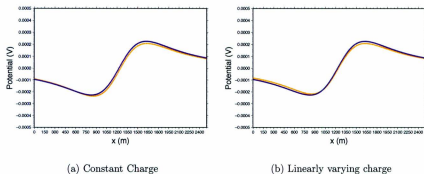


Figure 5.12: DC resistivity potential due to conductive buried sphere using pole-pole configuration for a source location of  $(-10000, 350, 0)$  m: analytic response (blue), 3D forward modelling code (orange).

### 5.5.2.3 Discretization effect on calculated potential

Here, results are presented for a calculated DC resistivity potential over a buried conductive sphere starting from a very coarse mesh which is gradually transformed to a very fine mesh. The current source is located at  $(-10000, 350, 0)$  m for all examples. As can be seen in Figs. 5.13 to 5.16, the larger the number of nodes and facets, the better the numerical solutions are. However, linearly varying charge approach was expected to produce a better response compared to the constant charge approach for a coarse discretization as the number of unknown variables is smaller.

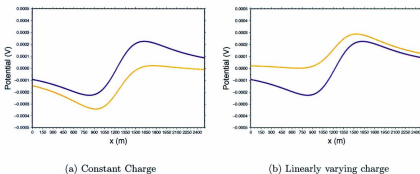


Figure 5.13: DC resistivity potential for the conductive buried sphere using a pole-pole configuration and using 94 facets and 49 nodes, analytic response (blue), 3D forward modelling code (orange).

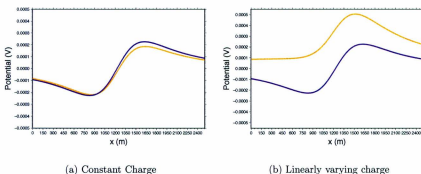


Figure 5.14: DC resistivity potential for the conductive buried sphere using a pole-pole configuration and using 304 facets and 154 nodes, analytic response (blue), 3D forward modelling code (orange).

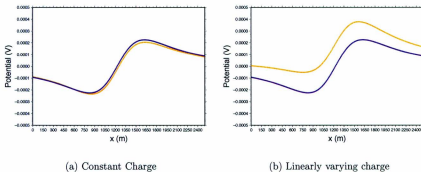
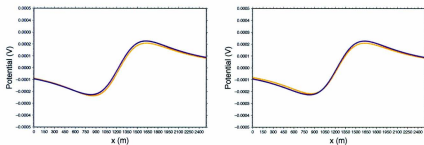


Figure 5.15: DC resistivity potential for the conductive buried sphere using a pole-pole configuration and using 1254 facets and 629 nodes, analytic response (blue), 3D forward modelling code (orange).



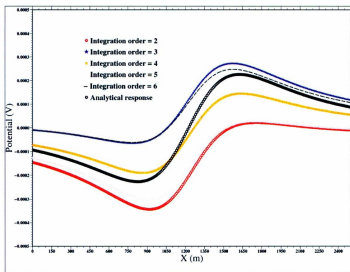
(a) Constant Charge

(b) Linearly varying charge

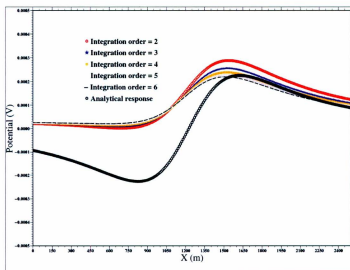
Figure 5.16: DC resistivity potential for the conductive buried sphere using a pole-pole configuration and using 1520 facets and 762 nodes, analytic response (blue), 3D forward modelling code (orange).

#### 5.5.2.4 Different orders of integration

The Gauss-Legendre quadrature method that is used to calculate the surface integral over an arbitrary oriented triangular facet (see eq. 5.56) can be implemented in different orders. An example is carried out to illustrate the effect of using different orders of integration on the final result. The current source is located at  $(-10000, 350, 0)$  m and two examples were used to compare the effect of integration order on both fine and coarse discretisations (see Figs. 5.17 and 5.18). The results shows that the order of integration has really no effect on how accurate the solution is when the fine discretisation is used. Since the computation time escalates as the order of integration increases, it makes sense to use lower order of integration.

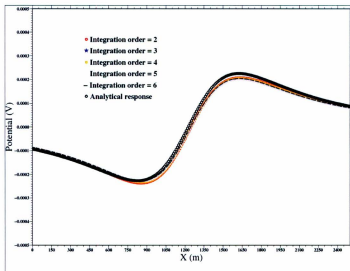


(a) Constant Charge

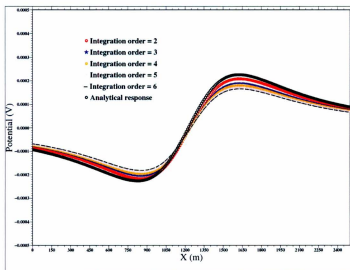


(b) Linearly varying charge

Figure 5.17: Different orders of integration for an sphere discretized into 94 facets and 49 nodes.



(a) Constant Charge



(b) Linearly varying charge

Figure 5.18: Different orders of integration for an sphere discretized into 1520 facets and 762 nodes.

## 5.6 Example 2: Potential due to a buried conductive prism

The other reference used to test the developed 3D surface integral code was the DCIP3D software package. DCIP3D forward modelling is based on the finite difference method and has been developed for structured regular rectangular cells. Two different 3D meshes were designed for 3D DC resistivity forward modelling using DCIP3D (see Chapter 4). One coarse mesh called mesh B with cells of dimensions  $50 \times 50 \times 50$  m and a finer mesh called mesh A with cells of dimensions  $25 \times 25 \times 25$  m (see section 4.2.1). The Earth model is a homogeneous half-space of conductivity  $10^{-4}$  S/m and chargeability of 0. A conductive prism of conductivity 1 S/m and chargeability of 0 is embedded. The extent of the prism was from  $x = 1150$  to 1300 m,  $y = 250$  to 450 m, and  $z = -400$  to  $-700$  m. For simplicity, the pole-pole configuration was again used. The current electrode was placed at  $(-300, 225, 0)$  m. Synthetic data were produced for a single profile from  $(0, 225, 0)$  m to  $(2500, 225, 0)$  m with the stations every 10 m. Using TetGen (Si, 2003), unstructured triangular meshes were produced with different numbers of nodes and facets defining the surface of the prism and these were used as input to the developed 3D forward modelling code (see Fig. 5.19). Figs. 5.20 to 5.25 show that the larger the numbers of nodes and facets, the better the numerical solutions. The computation time for a coarse mesh is in the order of several seconds and for a fine mesh is in the range of a couple of minutes. The linearly varying charge approach was expected to work better for the coarse meshes with small number of nodes and cells; however, the constant charge

approach gives better results for coarse meshes. In the case of fine mesh, the linearly varying charge approach produces better results.

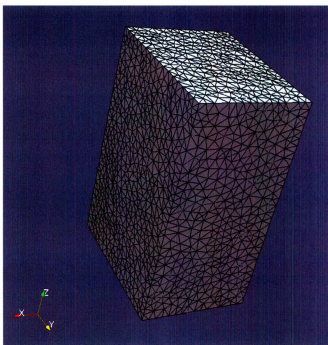
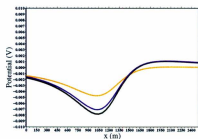


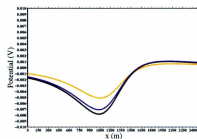
Fig. 5.19: Discretized prism using unstructured linear triangular facets with the extension of  $x = 1150$  to  $1300$  m,  $y = 250$  to  $450$  m, and  $z = -400$  to  $-700$  m and discretized into 4106 facets and 2055 nodes.



(a) Discretized prism

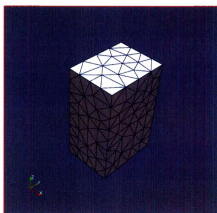


(b) Constant Charge

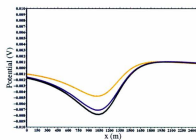


(c) Linearly varying charge

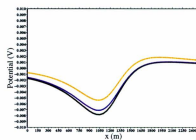
Figure 5.20: DC resistivity potential due to a conductive prism using the pole-pole configuration and observation locations along the  $x$ -axis, and 28 facets and 16 nodes: DCIP3D Mesh A (blue), Mesh B (black), 3D Forward modelling code (orange).



(a) Discretized prism

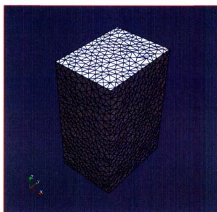


(b) Constant Charge

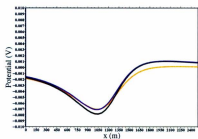


(c) Linearly varying charge

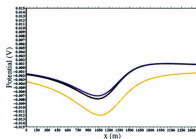
Figure 5.21: DC resistivity potential due to a conductive prism using the pole-pole configuration and observation locations along the  $x$ -axis, and 296 facets and 150 nodes: DCIP3D Mesh A (blue), Mesh B (black), 3D Forward modelling code (orange).



(a) Discretized prism

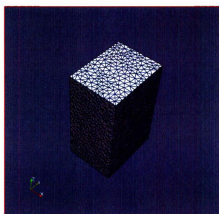


(b) Constant Charge

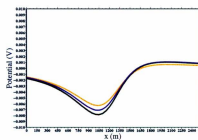


(c) Linearly varying charge

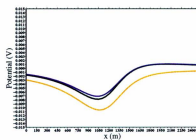
Figure 5.22: DC resistivity potential due to a conductive prism using the pole-pole configuration and observation locations along the  $x$ -axis, and 2646 facets and 1325 nodes: DCIP3D Mesh A (blue), Mesh B (black), 3D Forward modelling code (orange).



(a) Discretized prism

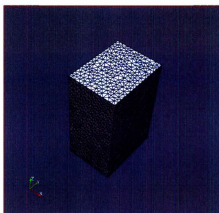


(b) Constant Charge

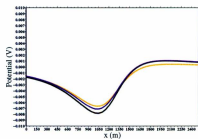


(c) Linearly varying charge

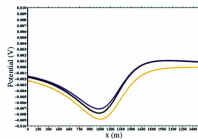
Figure 5.23: DC resistivity potential due to a conductive prism using the pole-pole configuration and observation locations along the  $x$ -axis, and 3068 facets and 1536 nodes: DCIP3D Mesh A (blue), Mesh B (black), 3D Forward modelling code (orange).



(a) Discretized prism

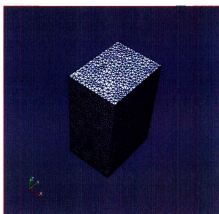


(b) Constant Charge

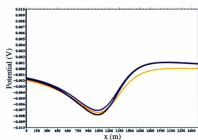


(c) Linearly varying charge

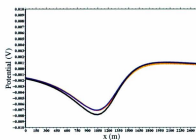
Figure 5.24: DC resistivity potential due to a conductive prism using the pole-pole configuration and observation locations along the  $x$ -axis, and 4106 facets and 2055 nodes: DCIP3D Mesh A (blue), Mesh B (black), 3D Forward modelling code (orange).



(a) Discretized prism



(b) Constant Charge

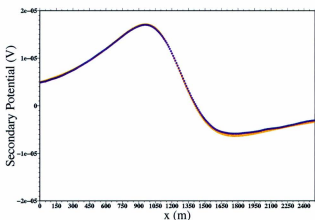


(c) Linearly varying charge

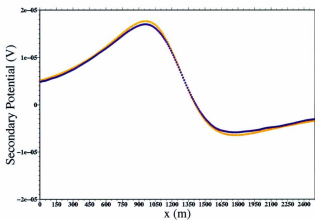
Figure 5.25: DC resistivity potential due to a conductive prism using the pole-pole configuration and observation locations along the  $x$ -axis, and 5744 facets and 2876 nodes: DCIP3D Mesh A (blue), Mesh B (black), 3D Forward modelling code (orange).

### 5.7 IP response due to a buried polarisable prism

The IP response as a secondary potential can be derived by performing two 3D DC forward modellings for a primary and disturbed conductivity based on the Siegel's theory. Assume that the polarisable cube now has a chargeability of 0.1 and is embedded in a non-polarisable half-space. There is no conductivity contrast between the cube and the surrounding region. The conductivity of the half-space is assumed to be  $10^{-3}S/m$ . All the settings and dimensions are as the same in the previous section. The IP results from the code are compared to the IP data produced by the 3D IP forward modelling of DCIP3D for both mesh A and B (see Figs. 5.26 and 5.27).

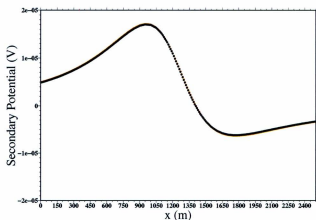


(a) Constant Charge

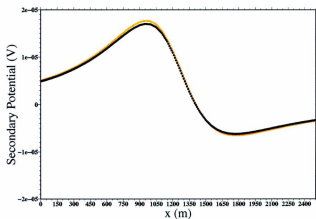


(b) Linearly varying charge

Figure 5.26: IP response as secondary potential due to polarisable buried cube using pole-pole configuration, DCIP3D Mesh A (blue), 3D forward modelling code (orange), 4106 facets and 2055 nodes



(a) Constant Charge



(b) Linearly varying charge

Figure 5.27: IP response as secondary potential due to polarisable buried cube using pole-pole configuration, DCIP3D Mesh B (black), 3D forward modelling code (orange), 4106 facets and 2055 nodes

## Chapter 6

### Conclusion

The classical borehole IP method for mineral exploration uses a lateral probe where the two potential electrodes and one current electrode are deployed in one probe and used to measure the voltage in the drill-hole. The other current electrode is placed on the ground at infinity. Classical borehole IP has several limitations including an investigation radius that is restricted by borehole depth, depth of measurements limited by borehole depth, sensitivity to in-hole mineralization and data that are not suited to 3D inversion. In this thesis, numerical modelling and inversion methods for the measurements of a novel IP borehole survey design have been investigated. The new survey design is called hole-to-hole IP. It was introduced by Abitibi Geophysics and aims to compensate for the limitations of classical borehole IP especially in providing data that are suitable for 3D modelling and inversion. Different combinations of receivers and boreholes have been examined to obtain the economically optimum survey design including the minimum number of boreholes and receiver locations for a successful imaging of the chargeable ore body in a mineral exploration project. The examples presented in the first part of this thesis show that the hole-to-hole IP configuration is a powerful technique providing a useful set of data for 3D modelling

of ore bodies in mineral exploration industry in which the combination of two pairs of boreholes perpendicular to each other where the target is located in the middle of them can be employed as an optimum and economical design for the hole-to-hole method with measurements made every 20 meters down the boreholes. Also, distance weighting applied during inversions improved the imaging of the mineral deposit located between boreholes. The best value for  $\beta$  (see eq. 4.1) was found to be 0.25 for inversion of hole-to-hole IP data. In the second part of the thesis, a 3D numerical technique based on the surface integral equation approach for modelling of DC resistivity and IP data was developed. The pivotal novelties in the code are, first, the application of unstructured meshes which are more flexible for representing realistic subsurface structures than structured meshes. Second, the 3D code has been developed for both situations of constant and linearly variable charge on each facet which enables the charge accumulation to be simulated over the boundary surface more precisely. Therefore, the developed code will enable numerical modelling to be done for more complicated ore bodies than was previously the case. All tests showed that the developed code produced accurate results (see Figs. 5.26 and 5.27). However, the linearly varying charge approach did not produce more accurate results for coarse meshes than the constant charge approach which was contrary to expectations.

## Bibliography

Alfano, L., 1959. Introduction to the interpretation of resistivity measurements for complicated structural conditions. *Geophysical Prospecting* 7, 311-366.

Alfano, L., 1960. The influence of surface formations on the apparent resistivity values in electrical prospecting, part 1. *Geophysical Prospecting* 8, 576-606.

Alfano, L., 1961. The influence of surface formations on the apparent resistivity values in electrical prospecting, part 2. *Geophysical Prospecting* 9, 213-241.

Beasley, C.W., and Ward, S.H., 1986. Three-dimensional mise-a-la-masse modeling applied to mapping fracture zones. *Geophysics* 51, 98-113.

Berube, P., 2010, Hole to Hole 3D Induced Polarization Solution, PDAC Symposium, Toronto, Ontario, Canada.

Bhattacharya P.K. and Patra H.P. 1968. Direct Current Geoelectric Sounding: Principles and Interpretations. Volume 9 of *Methods in Geochemistry and Geophysics*. Elsevier Science Publishing Co.

Boulanger, O., and Chouteau, M., 2005, 3D modelling and sensitivity in DC resistivity using charge density, *Geophysical Prospecting*, 2005, 53, 579-617.

Boyd, T.M., 2003, *Introduction to Geophysical Exploration*.

Coggon, J. H., 1971, Electromagnetic and electric modeling by finite-element method: *Geophysics*, 36, 132-155.

DCIP3D Manual, UBC-Geophysical Inversion Facility, Department of Earth and Ocean Sciences, University of British Columbia. Vancouver, British Columbia.

Dey, A. and Morrison, H. F., 1979. Resistivity modelling for arbitrarily shaped three-dimensional structures, *Geophysics*, 44, 753780.

Dieter, K., Paterson, N. R., and Grant, F. S., 1969, IP and resistivity type curves for three-dimensional bodies: *Geophysics*, v. 34, p. 615-632.

Dobrin, 1960, *Geophysical Prospecting*, New York, McGraw-Hill.

Farias, C., Maranhão, M., Rocha, B., and Andrade, N., 2010, Induced polarization forward modelling using finite element method and the fractal model, *Applied Mathematical Modelling* 34, 1849-1860.

Fink, J.B., Sternberg, B.K., McAlister, E.O., Weiduwilt, W.G. and Ward, S.H, *Induced Polarization, Applications and Case Histories, Investigations in Geophysics, Society of Exploration Geophysicists, Vol4, 1990.*

GRAV3D Version 3.0 , A Program Library for Forward Modelling and Inversion of Gravity Data over 3D Structures , UBC-Geophysical Inversion Facility, Department of Earth and Ocean Sciences, University of British Columbia, 2005.

Herman, R., 2001, An Introduction to Electrical Resistivity in Geophysics, *American Journal of Physics*, Volume 69, Issue 9, pp. 943

Hohmann G.W. 1975. Three-dimensional induced polarization and electromagnetic modeling. *Geophysics* 40, 309-324.

Hvozda M. and Kaikkonen P. 1998. An integral equations solution of the forward D.C. geoelectric problem for a 3-D body of inhomogeneous conductivity buried in a halfspace. *Journal of Applied Geophysics* 39, 95-107.

Jeffry, A., and Dai. H. H., 2008, Handbooks of Mathematical Formulas and Integrals, Fourth Edition, Elsevier.

Jin, J., 2002, The Finite Element Method in Electromagnetics, 2nd edition, John Wiley Sons, Inc.

Kaufman, A.A. and Anderson, B.I., 2010, Principle of electric Methods in Surface and Borehole Geophysics, Elsevier.

Li, Y., and Oldenburg, D.W., 1991. Aspects of charge accumulation in DC resistivity experiments. Geophysical Prospecting 39, 803-826.

Li, Y. and Oldenburg, D. W., 1998, 3D inversion of gravity data, Geophysics, 63, 109-119.

Li, Y. and Oldenburg, D. W., 2000, 3-D inversion of induced polarization data, Geophysics 65, 1931-1945.

Y. and Oldenburg, D. W., 2000, Joint inversion of surface and three-component borehole magnetic data, Geophysics, Vol. 65, N0. 2.

Loke, M.H., 1999, Electrical imaging surveys for environmental and engineering studies, Unpublished Short Training Course Lecture Notes. Geotomo Software, Penang, Malaysia, 65 pp.

MAG3D, A Program Library for Forward Modelling and Inversion of Magnetic Data over 3D Structures VERSION 4.0, UBC-Geophysical Inversion Facility, Department of Earth and Ocean Sciences, University of British Columbia, 2005.

Moore, S., Baker, A.J., Dongarra, J., Halloy, C., and Chung Ng, 2002, Active Netlib: An Active Mathematical Software Collection for Inquiry-based Computational Science and Engineering Education, Journal of Digital Information, Vol 2, No 4.

Mufti, I.R., 1976. Finite-difference resistivity modeling for arbitrarily shaped two-dimensional structures, Geophysics, 41, 62-78.

Mwenifumbo, C.J., 1997, Electrical methods for ore body delineation, paper 95, Geological survey of Canada, Proceedings of Exploration 97: Forth Decennial International Conference on mineral exploration.

Okabe, M., 1979, Analytical expressions for gravity anomalies due to homogeneous polyhedral bodies and translations into magnetic anomalies, Geophysics, Vol.34, No.4, P. 730-711.

Parasnis, D.S., 1997, Principle of Applied Geophysics, Fifth edition, Chapman and Hall.

Pelton, W.H., Ward, S.H., Hallof, P.G., Sill, W.R. and Nelson, P.H., 1978. Mineral discrimination and removal of inductive coupling with multifrequency IP, Geophysics, 43, 588-609.

Poirmeur C. and Vasseur G. 1988. Three-dimensional modeling of a hole-to-hole electrical method: Application to the interpretation of a field survey. Geophysics 53, 402-414.

Pratt, D.A., 1972. The surface integral approach to the solution of the 3D resistivity problem. Bulletin of the Australian Society for Exploration Geophysics 3, 33-50.

Qian, W., Milkereit, B., McDowell, G., Stevens K. and Halladay, S., 2007, Borehole Resistivity Logging and Tomography for Mineral Exploration.

Raiche, A.P., 1974. An integral equation approach to three-dimensional modelling. *Geophysical Journal of the Royal Astronomical Society* 36,363-376.

Rathod, H.T., Nagaraja, K.V., and Venkatesudu, B., 2007, Symmetric Gauss-Legendre quadrature formulas for composite numerical integration over a triangular surface, *Applied Mathematics and Computation*, 188, 865876.

Rubin, Y., and Hubbard, S.S., 2005, *Hydrogeophysics*, Peter Wilderer (ed.) *Treatise on Water Science*, vol. 1, pp. 401-434 Oxford: Academic Press, 2011

Schulz, R., 1985. The method of integral equation in direct current resistivity method and its accuracy. *Journal of Geophysics* 56, 192-200.

Sharma, P.V., 1997, *Environmental and Engineering Geophysics*, Cambridge University Press.

Si, H., 2003, Tetgen, a quality tetrahedral mesh generator and 3D Delaunay triangulation: <http://tetgen.berlios.de>, accessed 01 July 2006.

Siegel, H.O., 1959. Mathematical formulation and type curves for induced polarization, *Geophysics*, 24, 547-565.

Snyder D.D. 1976. A method for modeling the resistivity and IP response of two-dimensional bodies. *Geophysics* 41, 99-1015.

Spiegel R.J., Sturdivant V.R. and Owen T.E. 1980. Modeling resistivity anomalies from localized voids under irregular terrain. *Geophysics* 45,1164-1183.

Sumner, J.S., 1976, *Principles of Induced Polarization for Geophysical Exploration*, Elsevier Science Ltd.

Telford, W.M., Geldart, L.P., Sheriff, R.E. and Keys, D.A., 1976, Applied Geophysics, Cambridge University Press.

Ting, S., and Hohmann, W., 1981. Integral equation modeling of three-dimensional magnetotelluric response. *Geophysics* 46, 1821-197.

Vanhala, H., Soininen, H. and Kukkonen, I., 1992. Detecting organic chemical contaminants by spectral-induced polarization method in glacial till environment, *Geophysics*, 57, 1014-1017.

Wannamaker, P., Hohmann, G., and SanFilipo, W., 1984. Electromagnetic modeling of three-dimensional bodies in layered earths using integral equations. *Geophysics* 49, 60-74.

Weller, A., and Borner, F.D., 1996. Measurements of spectral induced polarization for environmental purposes, *Environmental Geology*, 27, 329-334.

Weller, A., Seichter, M., and Kampke, A., 1996. Induced-polarization modelling using complex electrical conductivities, *Geophys. J. Int.*, 127,387-398.

Xiong Z. 1989. Short note: Electromagnetic fields of electric dipoles embedded in a stratified anisotropic earth. *Geophysics* 54, 1643-1646.

Xiong Z. 1992a. Electromagnetic modeling of 3-D structures by the method of system iteration using integral equations. *Geophysics* 57, 1556-1561.

Xiong, Z., 1992b. Short note: Symmetry properties of the scattering matrix in 3-D electromagnetic modeling using the integral equation method. *Geophysics* 57, 1199-1202.

Zhou, B., and S. A. Greenhalgh, 2001, Finite-element 3D direct current resistivity modeling; accuracy and efficiency considerations: *Geophysical Journal International*, 145, 679-688.

Zonge, K., 1993, *Geophysical Prospecting Method*, The journal of the Alaska Miners Association, Inc. 501 West Northern Lights Blvd., Suite 203, Anchorage, Alaska 99503.

## Appendices

## Appendix A : Gaussian Abscissas and Weights

Table 1: Gaussian Abscissas and Weights

$n$	$k$	$x_k^n$	$\omega_k^n$
2	1	0.5773502629	1.0000000000
	2	-0.5773502629	1.0000000000
3	1	0.7745966692	0.5555555555
	2	0.0000000000	0.8888888888
	3	-0.7745966692	0.5555555555
4	1	0.8611363116	0.3478548451
	2	0.3399810436	0.6521451549
	3	-0.3399810436	0.6521451549
	4	-0.8611363116	0.3478548451
5	1	0.9061798459	0.2369268850
	2	0.5384693101	0.4786286205
	3	0.0000000000	0.5688888889
	4	-0.5384693101	0.4786286205
	5	-0.9061798459	0.2369268850
6	1	0.9324695142	0.1713244924
	2	0.6612093865	0.3607615730
	3	0.2386191861	0.4679139346
	4	-0.2386191861	0.4679139346
	5	-0.6612093865	0.3607615730
	6	-0.9324695142	0.1713244924

## **Appendix B : 3D Forward Modelling Code for DC resistivity and IP data**

Details on the developed 3D forward modelling code for DC resistivity and IP data in Chapter 5 can be found in the CD attached to the thesis.





